

## Article

# Annual Coastal Boulder Mobility Detected in 2017–2021 Remote Sensing Imagery and Its Relation to Marine Storms (Gulf of Taranto, Mediterranean Sea)

Marco Delle Rose 

National Research Council of Italy, Institute of Atmospheric Sciences and Climate, 73100 Lecce, Italy; marco.dellerose@cnr.it

**Abstract:** Landward displacements of coastal boulders are geomorphological signatures of sea flooding and erosion processes. In this study, using open-access resources that do not require the integration of specialist software, the 2017 to 2021 annual mobility of medium, coarse, and very coarse boulders spread over about 100 km of the eastern coast of the Gulf of Taranto (Italy, Mediterranean Sea) was explored. The boulder displacement data obtained from remote sensing imagery were verified and refined by means of geomorphological field investigation. The main results are the following: (1) A large interannual variability in the boulder mobility was found; (2) storm Detlef, which crossed over the Mediterranean during 11–13 November 2019, was recognized as the cause of a massive displacement phenomenon; and (3) the marine weather conditions driving the investigated morphodynamic process were inferred.

**Keywords:** open access resources; comparative visual analysis; geomorphological investigation; overtopping flow; Ionian Sea; Apulia region; storm Detlef



**Citation:** Delle Rose, M. Annual Coastal Boulder Mobility Detected in 2017–2021 Remote Sensing Imagery and Its Relation to Marine Storms (Gulf of Taranto, Mediterranean Sea). *Geosciences* **2024**, *14*, 136. <https://doi.org/10.3390/geosciences14050136>

Academic Editors: Aggeliki Kyriou, Lia Bárbara Cunha Barata Duarte, Christos Pikridas and Jesus Martinez-Frias

Received: 12 April 2024

Revised: 10 May 2024

Accepted: 13 May 2024

Published: 15 May 2024



**Copyright:** © 2024 by the author. Licensee MDPI, Basel, Switzerland. This article is an open access article distributed under the terms and conditions of the Creative Commons Attribution (CC BY) license (<https://creativecommons.org/licenses/by/4.0/>).

## 1. Introduction

In several coastal areas, different-sized boulders are transported and emplaced above the sea level by waves that surge over the coastline like land-crossing bores. Massive displacements of large clasts are geomorphological signatures of flooding events due to severe storms and tsunamis [1–4]. Since about a decade, specific bands available with commercial Earth observation satellites such as WorldView-2 have allowed the definition of geomorphological and morphometric features of coastal deposits in detail [5,6]. The open access to high-resolution remote sensing imagery via the web-interface provided by Google Earth (GE) has greatly increased the possibilities of understanding boulder formation and mobility [7–9]. The dynamics and morphometry of displaced clasts can help to assess the wave energy on the coast, an important focus of research in physical geography and in applied sciences such as engineering and coastal management [1,2,9].

Boulder mobility accounts for the number of boulders displaced over a stretch of coast by water flows during a given time interval. It has attracted the attention of several scholars in recent years and has been used for various purposes, for example, to test hydrodynamics equations that govern the boulder displacement [10], to explore the ability of contemporary storms to cause geomorphological changes on rocky coasts [11], and to investigate the relationship among transport distance and storm frequency and intensity [12]. Moreover, the measure of the mobility of coastal boulders over pluriannual periods has been addressed in several studies to explore sedimentological features (see, e.g., [13,14]).

By means of geomorphological survey and comparing two sets of very-high-resolution (VHR) imagery provided by GE, Delle Rose et al. [9] recognized a massive displacement phenomenon (involving many dozens of large boulders) that occurred between July 2018 and June 2020 along the 100 km eastern coast of the Gulf of Taranto (southern Apulia region, Italy, central Mediterranean; see Figure 1). These authors considered two storms (Vaia,

which occurred on 28–29 October 2018, and Detlef, which occurred on 12–13 November 2019, respectively; see references [15,16] for their synoptic framework) as possible causes for such an impressive displacement of boulders.

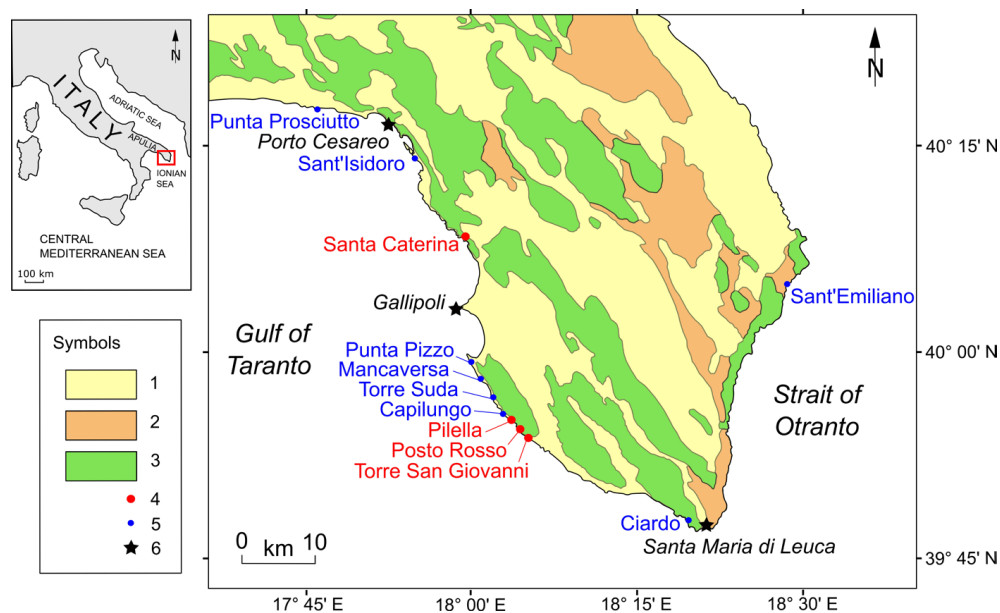


**Figure 1.** Geological map of the study area (after [9], modified). Symbols: 1, Quaternary rocks (carbonates, bioclastic deposits, marls); 2, Tertiary rocks (carbonates, marls); 3, Cretaceous rocks (limestones, dolostones); 4, site of boulder displacement detected in this study (see text); 5, site of boulder displacement detected by [9]; 6, wind gauge station.

The present work is a continuation of previous studies [4,9,17]. Its aims were three-fold: (1) determine the annual mobility of large boulders along the coast in Figure 1 over 4 years (from 2017 fall to 2021 summer), (2) establish whether one of the two mentioned storms can be ruled out as cause of the massive displacement phenomenon, and (3) infer the marine weather conditions driving the investigated morphodynamic process.

## 2. Materials and Methods

### 2.1. Study Area

The Gulf of Taranto faces the north Ionian Sea for more than 330 km (Figure 1) and is characterized by a microtidal regime with an astronomical tides of 0.3 m. For such a semi-enclosed basin, maximum significant waves of 6.3 m for a 50-year return period and of 8.2 m for a 100-year return period were calculated, respectively [18,19]. Along the low-lying eastern side of the gulf, jointed carbonate rocks extensively outcrop. These rocks are shaped by typical coastal karst forms including solution pans and pinnacles. The coast is prone to boulder formation and displacement, and because of such characteristics, two selected sites (namely Sant'Isidoro and Torre Suda; see Figure 1) have been periodically surveyed with direct observation since 2017 [17,20,21]. Careful geomorphological surveys are performed especially after the more severe storms.

The two 6-month climatic seasons of October–March (cold–wet, CW) and April–September (warm–dry, WD) characterize the Mediterranean climate over the Gulf of Taranto [22,23]. Indeed, the southwards migration of the Atlantic storm track and the descending mid-atmospheric troughs from Northern Europe are typical of the CW season, while good weather with scarce precipitation prevails from April to September. The Apulia region is characterized by the predominance of northerly winds, although winds from the south are significant for frequency and strength [24]. The Gulf of Taranto is exposed to strong winds generated by the seasonal prevalence of the anticyclones. Typical local storms in the central Mediterranean Sea are usually driven by middle-atmosphere

low-pressure centers (troughs in the 500 hPa GPH weather maps) generally following a NW-to-SE path [23]. Their income is characterized by southerly warm currents over the south Mediterranean Sea that can cause strong surface winds, according to the position of the surface pressure minima, especially in fall season. These meteorological conditions can cause, in turn, quite high waves above the southern Apulia coasts because of their potentially long geometrical fetch southwards to the Africa coasts and in accordance with their duration [17,25].

## 2.2. Remote Sensing Data and Geomorphological Survey

A challenge for this work was to explore the potential of physical geography investigations based on publicly available remote sensing sources and simple and inexpensive methods. Open-access resources that do not require the integration of specialist software such as GE have proven particularly effective in geomorphological research [8,26,27]. Since the first availability of very-high-resolution (sub meter) satellite images (produced by Airbus Defence and Space, Maxar Technologies, and other space technology companies), the online measuring tools of GE have been used to measure the horizontal dimensions of the boulders as well as their transport distance [28–30]. On the other hand, the horizontal accuracy of the images made available in the last few years has been tested on several geographic regions (see, e.g., [31,32]). For the Italian territory, the use of VHR GE images in geomorphology and other disciplines focused on the physical sciences has also been successfully explored (see, e.g., [33–35]).

To detect the morphometric features of the boulders and their mobility at annual scale, the eastern coast of the Gulf of Taranto was visually examined using the four last sets of VHR remote sensing images available on GE (dated July 2017, July 2018, June 2020, and September 2021, respectively) and a set of aerial images (taken during July 2019 at an average flight altitude of 180 m) that was recently made available by the governmental Authority of Apulia at the site “Territorial Planning Service” [36] (*Servizio Assetto del Territorio*, in Italian). The last set allowed us to fill the time gap (i.e., the 2019 summer) of the GE sets series. The visual analysis was performed according to the rudiments of geographic object-based image analysis (GEOBIA) [37]. The comparison between GE and regional aerial images [36] was carried out by means of QGIS software. It must be noted that the use of GE tools and QGIS functions to map large boulders and detect their mobility has been discussed and tested by several authors (see, e.g., [38–40]). Once determined from GE the geographical coordinates, the studied objects were easily found in the field by means of global positioning system (GPS) devices. The on-site geomorphological survey was carried out for the following aims: to verify and refine the morphometric data obtained from the remote sensing imagery; to determine the lithology of the boulders; and to infer, where possible, pre-transport setting and movement type (Appendix A).

## 2.3. Methodological Descriptions

Boulders usually are complex solids [41–43]. However, in the first stage of the geomorphological investigation, a boulder is considered an idealized-shaped rectangular cuboid, with the size described by the dimension of its axes:  $a$  (major),  $b$  (middle), and  $c$  (minor). The axes dimensions can be used to establish the flatness index (FI) =  $(a + b)/2c$  and the shape (Sh) of the boulders [44,45]. According to the Udden–Wentworth grain-size scale, boulders range from the class of fine boulders, with a middle axis > 0.25 m, to the class of medium blocks, with a middle axis of up to 16.4 m [45]. The middle axis ranges from 0.5 to 1 m for medium boulders, from 1 to 2 m for coarse boulders, and from 2 to 4.1 m for very coarse boulders. Based on the resolution of the used remote sensing images, attention was focused on medium to very coarse boulders. The boulder demarcation was manually performed, taking care to consider the shadowing conditions since the shape of such an object may seemingly change depending on the shadows cast at different times of the day [46].

Following the approach of previous studies [8,30,47], visual analysis was performed at an eye elevation of 50 to 200 m. Using GE, the two axes of the boulder presented as upward-facing in the images can be measured by the ruler tool. They are designated as the apparent major ( $a_r$ ) and medium axes ( $b_r$ ), with the minor axis being usually perpendicular to the image [28–30]. Actually, since the boulders may be inclined rather than horizontal,  $a_r$  and  $b_r$  are equal or smaller than the major and middle axis, respectively. Dealing with boulder displacement, other geometrical features that can be obtained using a computer workstation are the initial ( $x_i$ ) and final distances ( $x_f$ ) of the boulders from the coastline and the related transport distance (TD). The geographical coordinates of  $x_i$  and  $x_f$  were taken by estimating the positions of the geometric center point in the VHR GE images. Then, the TD (i.e., the joining line between the two positions) was measured using the ruler tool.

In the previous work [9], the difference between the measurements of displacement taken with GE's ruler tool and the ones carried out during a field survey with a measuring tape rarely exceeded 5%. Given this accuracy, in this study, the TDs were obtained, in a practical way, by measuring the distances between  $x_i$  and  $x_f$  in GE images. Several measures of TD were taken also in the field (see examples in Appendix A), with the aim of further testing the difference between the two types of measurements. The quality of the aerial images available at the site [36], as visualized in QGIS, was adequate to compare shape and position of the displaced boulders with those shown in the GE images. It must be noted that similar techniques have already been used successfully in previous studies (see, e.g., [47,48]).

The use of GPS devices allowed us to quickly identify the boulders at the respective  $x_f$  and thus to detail the morphometric features inferred from the remote sensing analysis. The prints left on the platform at the  $x_i$  by the displaced boulders were recognized in the same easy manner. Where the boulder was detached from the parent rock, the trace (called the socket; see ref. [49]) consists of a fresh and un-weathered rock surface not yet covered by lichen. The print left by a boulder that has already been uprooted from its geological substrate and has been lying on the ground for some time (i.e., the sub-aerial pre-transport setting; see Appendix A) can be detectable for some years under favorable sunlight conditions before being covered by lichen [9].

Surface karst forms such as solution pans and pinnacles have been used to establish the pre-transport setting and movement type for several boulders [9,17]. These inferences are based on the fact that fresh and un-weathered faces of boulders are indicative of the absence of karst processes before displacement (see examples in Appendix A). Also, ephemeral tracks (they are usually visible for only a few years) recognizable during the field geomorphological investigation, like the drag and impact marks [2,9,50], can give hints about the type of movement to which the boulders have been subjected. Finally, organic remains of marine plants covering the faces of displaced boulders suggest their initial submerged position.

To obtain an overview of the marine conditions in the eastern Gulf of Taranto during 2017–2021, publicly available datasets were examined. Special attention was given to the storminess conditions, which more than likely caused the landward boulder displacements. A marine storm is “a succession of sea states in which the significant wave height exceeds a fixed threshold for a duration of at least equal to 12 h” [51]. Moreover, to be relevant by the geomorphological point of view, a storm must have “the potential to significantly alter the underlying morphology and expose the backshore to waves, currents and/or inundation” [52].

The web archives of the GLOBO-BOLAM-MOLOCH model cascade were used to make a screening of the central Mediterranean 2017–2021 storms [53]. To identify the middle-atmosphere pressure conditions that allowed us to check the presence of stormy conditions, the 500 hPa geopotential height maps of the GLOBO model archive were carefully screened. Then, in order to obtain information about the offshore wind field (fetch length and direction, average wind speed at 10 m height, and storm duration) the archives of the mesoscale models BOLAM (10 km horizontal resolution) and MOLOCH (3 km horizontal resolution) were used. The storms were selected considering a minimum duration of 12 h

together with a minimum fetch usually greater than 500 km, alongside a minimum wind speed of 12 m/s throughout the considered time. These are typical conditions achieved by the storms affecting the Gulf of Taranto and correspond to significant wave heights generally above 3 m (sea state  $\geq 5$  of the Douglas sea scale). As performed in the previous work [9], using windstorm characteristics extracted by the BOLAM-MOLOCH model, the characteristic wave height  $H_0$  in the marine storms was calculated (see Appendix B).

The nearshore wind conditions during the storms, useful for completing the description of the weather features, were extracted from the datasets of the wind gauge stations placed along the studied stretch of coast (Figure 1). Finally, the minimum values of wave height theoretically capable of displacing the boulders were inferred from commonly used hydrodynamic equations [1,54–56] to relate the results of the present and previous works [9,17] (see Appendix B for details).

### 3. Results

The annual boulder mobility from fall 2017 to summer 2021 for the eastern coast of the Gulf of Taranto and the related marine conditions are reported below. The newly recognized displacements of medium to very coarse boulders are described in Section 3.1, while the multi-temporal check performed on the displacements recognized by [9] is shown in Section 3.2. The marine weather conditions and the main features of the storms for the above time interval are given in Section 3.3.

#### 3.1. New Detection of Boulder Displacement

Multi-temporal analysis allowed the recognition of 38 boulder displacements that occurred during the investigated time period, spread over four previously undetected sites (in red in Figure 1). In Table 1, these sites are reported from north to south. For 25 out of 38 boulders, both the pre- and post-transport positions were recognized; thus, the TD was established. To expose the physical geography results, selected images downloaded from both GE and the site [36] were elaborated in the Inkscape program (an open-source vector graphics editor).

**Table 1.** Acronym code (ID Code), number of identified Boulders, and number of established transport distances (No. of TD).

Site Name	ID Code	Boulders	No. of TD
Santa Caterina	SC	2	1
Pilella	PIL	14	11
Posto Rosso	RO	16	10
Torre San Giovanni	SG	6	3

Numerical data and complementary field measures and observations are given in Appendix A. The initial and final coordinates of the displaced boulders are in Tables A1, A3, A5 and A7. The lengths of the boulder axes measured on VHR GE imagery and on-site, respectively, together with other features (inclination on the ground; initial and final distances from the coastline; transport distance; lithology; shape; flatness index; pre-transport setting; inferred type of movement) of the displaced boulders are in Tables A2, A4, A6 and A8.

The northernmost site, Santa Caterina, is quite far from the other three sites (about 25 km), while these latter are close together (a few kilometers from each other; Figure 1). The stretch of the coast of Santa Caterina is characterized by a vertical cliff up to 5 m high; differently, at the other new sites, the height above the sea level of the cliff edge ( $H_c$ ) rarely exceeds 1.5 m.

The two boulders displaced at Santa Caterina (Tables 1, A1 and A2) experienced different movements (Figure 2). SCa was positioned at the cliff edge at least up to July 2019. In its place, after June 2020, a socket is present (Figure A1 in Appendix A), while the detached boulder is not detectable in the images. Likely, it fell back onto the sea bottom

after the impact of a high-energy run-up wave. The socket is hardly visible in the September 2021 image, probably because of an unfavorable sunlight condition. The boulder SCb is clearly distinguishable, with respect to the surroundings, both in the July 2017 and July 2018 images. SCb was still in the same position in July 2019 (Figure 2a–c), while it showed a new position in both June 2020 and September 2021 (Figure 2d,e). Currently, it lies in a shrub vegetation area (Figure A2 in Appendix A). The displacement of SCb is quantifiable in a TD of about 15 m (Table A1) from SW to NE (Figure 2f). Both the SCa and SCb boulders were displaced between July 2019 and June 2020 (Figure 2c,d).

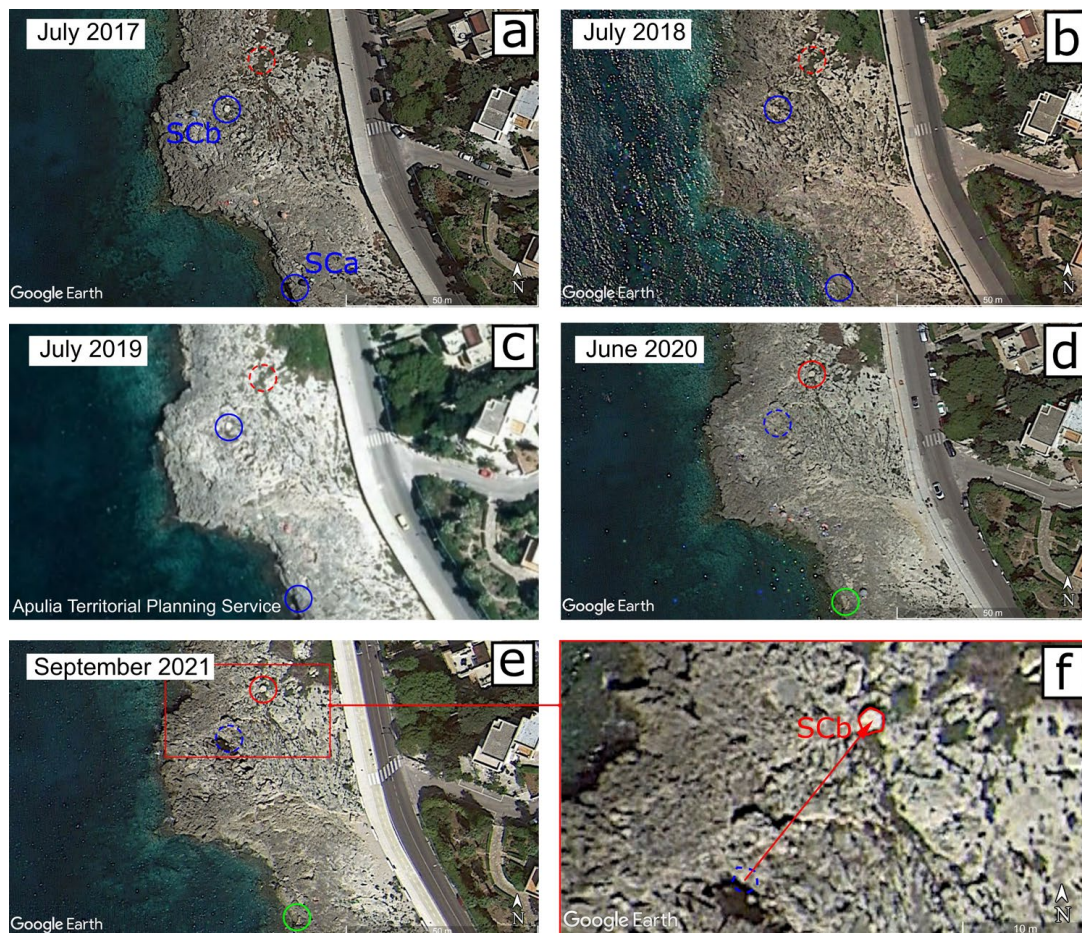


**Figure 2.** Santa Caterina coast ( $40^{\circ}08'16.93''$ – $40^{\circ}08'19.47''$  N,  $17^{\circ}59'16.11''$ – $17^{\circ}59'21.97''$  E) detection of boulder displacements: (a,b,d,e) GE images, eye elevation of 127 m; (c) regional aerial image; (f) transport vector of SCb boulder, eye elevation of 43 m. Blue symbols, pre-displacement position; red symbols, post-displacement position; green symbols, socket of boulder disappeared into the sea. Dotted lines help the comparison.

Along the stretch of the coast of Pilella (Figure 1 for location), 14 displaced boulders were identified by multi-temporal analysis. For 11 of these boulders, both the initial and final positions were detected and, thus, the TD calculated (Table 1). The middle axis ranges from 1 to 1.5 m, except for one case (PILj), which is nearly 2 m (Table A4); TD ranges from 1.5 to 5 m (Table A3), with vectors oriented about SSW–NNE. The initial positions of these 14 boulders do not change in the July 2017, July 2018, and July 2019 images; likewise, the final positions do not change in the June 2020 and September 2021 images. Two boulders of this site are inclined of  $55$ – $60^{\circ}$  with respect to the ground (Table A4). Such a geomorphological setting can make axis measurement from remote sensing images rather unreliable. As an example, for the PILn boulder (see Figure A3 for its arrangement on the coast),  $b_f$  was found to be one-third smaller than  $b_i$  (Table A4).

The northernmost boulders of the Pilella site are shown in Figure 3. Comparing the boulder shadow casts of the July 2017 to July 2019 images, detailed planar shapes of PILl, PILm, and PILn can be inferred (Figure 3a–c). In the June 2020 and September 2021 images, PILl, PILm, and PILn are overturned in comparison with the positions of the previous images (Figure 3d–f). Their exposed surfaces, not covered by lichen, are whitish and easily distinguishable from the surrounding gray texture. Consequently, they were overturned by water flow, roughly oriented SSW–NNE, between July 2019 and June 2020.

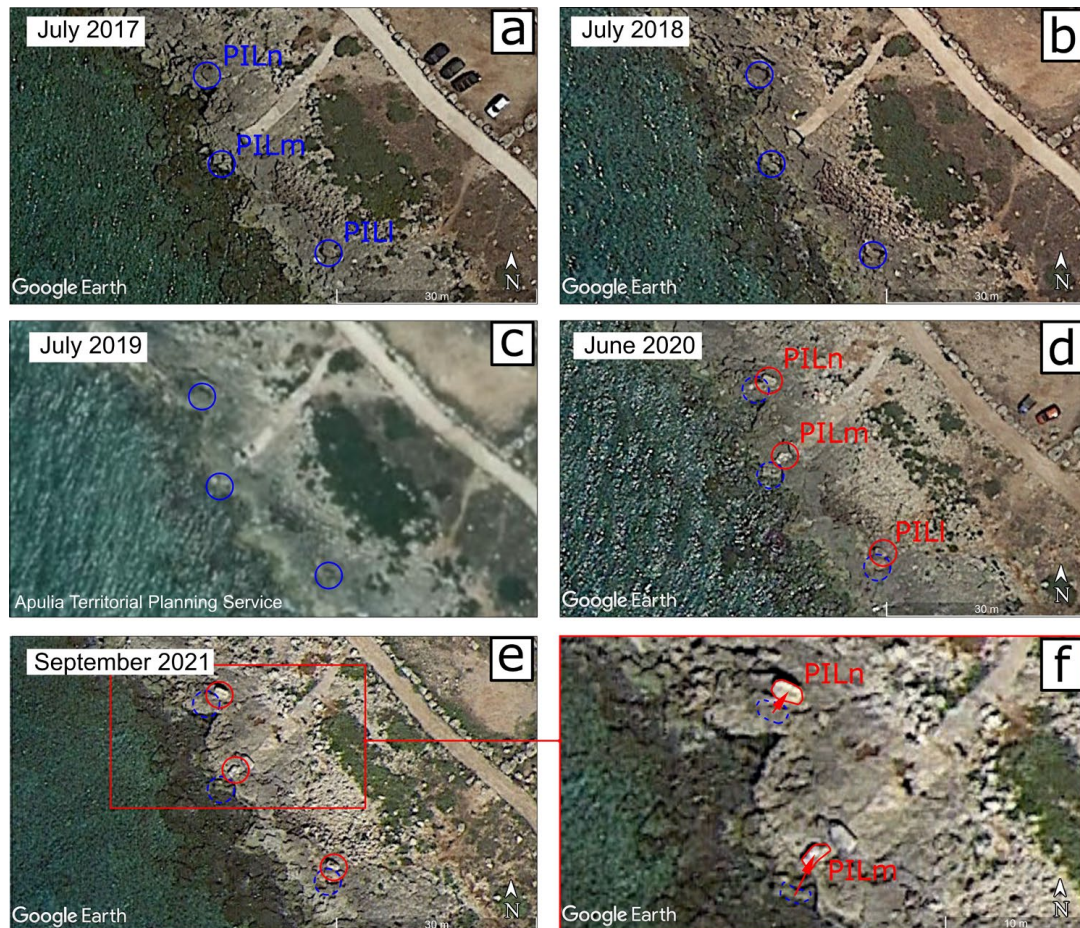


**Figure 3.** Pilella coast ( $39^{\circ}55'26.18''$ – $39^{\circ}55'27.61''$  N,  $18^{\circ}03'25.23''$ – $18^{\circ}03'28.54''$  E) detection of boulder displacements: (a,b,d,e) GE images, eye elevation of 73 m; (c) regional aerial image; (f) transport vector of PILm and PILn boulders, eye elevation of 38 m. Blue symbols, pre-displacement position; red symbols, post-displacement position. Dotted lines help the comparison.

The site of Posto Rosso, where 16 displaced boulders were identified (Table 1), is located about 1.5 km southeast of Pilella (Table A5). For 6 of these boulders, the initial position was not established, while the final position was established for all the 16 boulders. Their middle axis ranged from about 1 to 2 m and the transport distance from 2 to 17 m (Table A6); vectors are oriented about SSW–NNE. In Figure 4, the analyzed time series remote sensing images of the central sector of the stretch of the Posto Rosso coast are reported. Due to the different sun–boulder–sensor geometries of the July 2017 to July 2019 images, the planar shape of the boulders can be defined in detail (Figure 4a–c). The ROe, ROg, and ROh, boulders appear in the series of images taken since June 2020; instead, the ROI boulder appears after September 2021 (Figure 4d,e; see also Figure A5b in Appendix A for the geomorphological setting). The faces of these four boulders observed in the field were fresh and did not show solution microforms, while traces of organic remains of marine

plants were found. It follows that they were on the sea bottom before being displaced by waves (see Appendix A for submerged pre-transport setting).

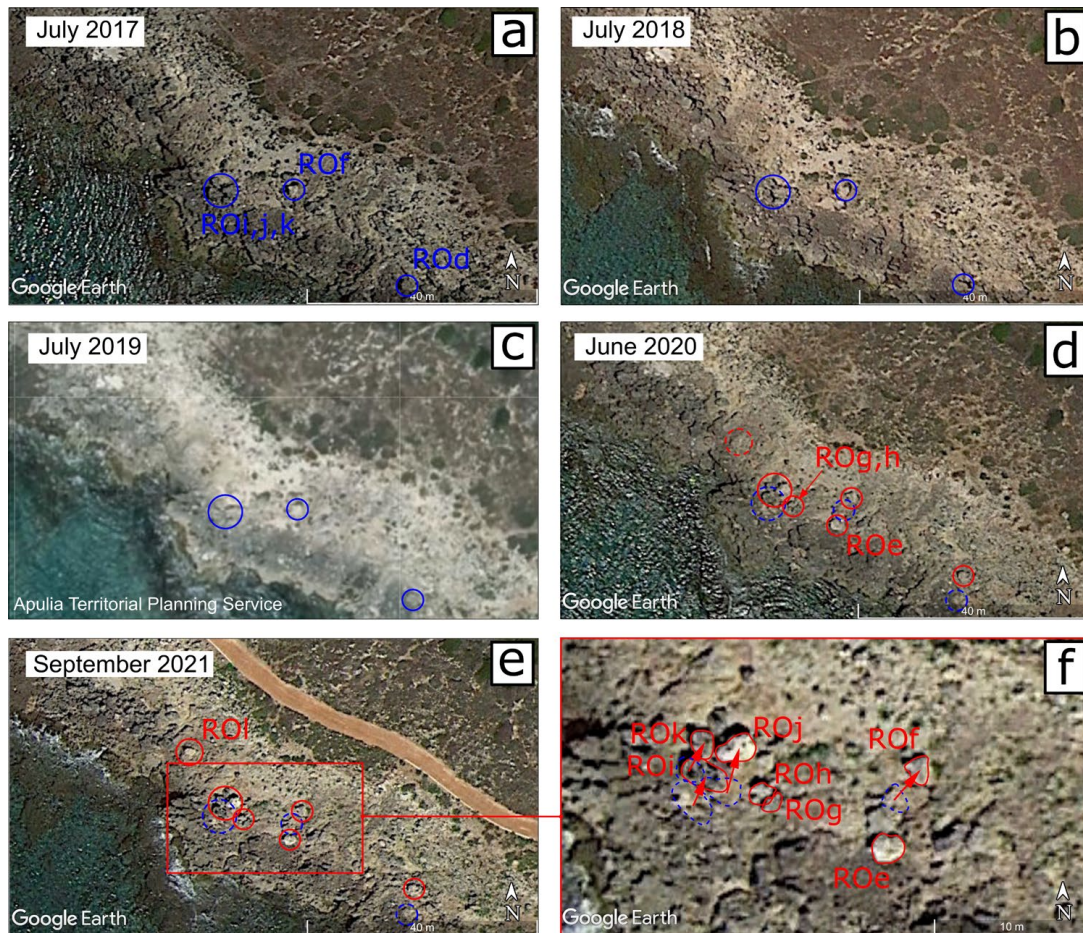


**Figure 4.** Posto Rosso coast ( $39^{\circ}54'47.70''$ – $39^{\circ}54'49.57''$  N,  $18^{\circ}04'15.79''$ – $18^{\circ}04'20.12''$  E) detection of boulder displacements: (a,b,d,e) GE images, eye elevation of 93 m; (c) regional aerial image; (f) transport vectors of ROi, ROj, and ROk boulders, eye elevation of 35 m. Blue symbols, pre-displacement position; red symbols, post-displacement position. Dotted lines help the comparison.

Except for the ROI boulder, the changes in position of the boulder displaced at the Posto Rosso site occurred between July 2019 and June 2020 (Figure 4c,d), while no changes apparently occurred between July 2017 and July 2018 (Figure 4a,b) and July 2018 and July 2019 (Figure 4b,c). Given the above, it can be inferred that the ROI boulder was emplaced above the sea level between June 2020 and September 2021. As a whole, among the four new sites, Posto Rosso is the one with the greatest number of displaced boulders. These calcarenite boulders were detached from a surface that corresponds to the stratigraphic contact with the limestone (see Figure A5a,c,d in Appendix A). Apparently, the stratigraphy here is crucial for the boulder formation.

The southernmost site identified by multi-temporal analysis is Torre San Giovanni (Figure 1 for location). For three out of the six boulders displaced, the pre-displacement position and TD were determined (Table A7). Their middle axis ranges from about 1 to more than 1.5 m (Table A8). The transport vectors are up to almost 10 m in length and approximately S–N oriented, as shown in Figure 5f. All the boulders of this site experienced position changes between July 2019 and June 2020 (Figure 5a–e). The SGc and SGd boulders have apparently completed their movement because they were stopped by other boulders lying on the coastal platform (Figure A6 in Appendix A).

On the displaced boulders whose initial position was not detected in the remote sensing images (Table A7), decaying organic matter (likely remains of marine plants) was observed. This suggests that they were in submerged conditions before being moved.

As a whole, visual analysis of the 2017–2021 time series remote sensing images allowed to establish that 37 out of 38 boulders of the newly detected sites were displaced between July 2019 and June 2020. One boulder (ROI; see above) changed position between June 2020 and September 2021. For 25 boulders, the TD was determined (Table A9).

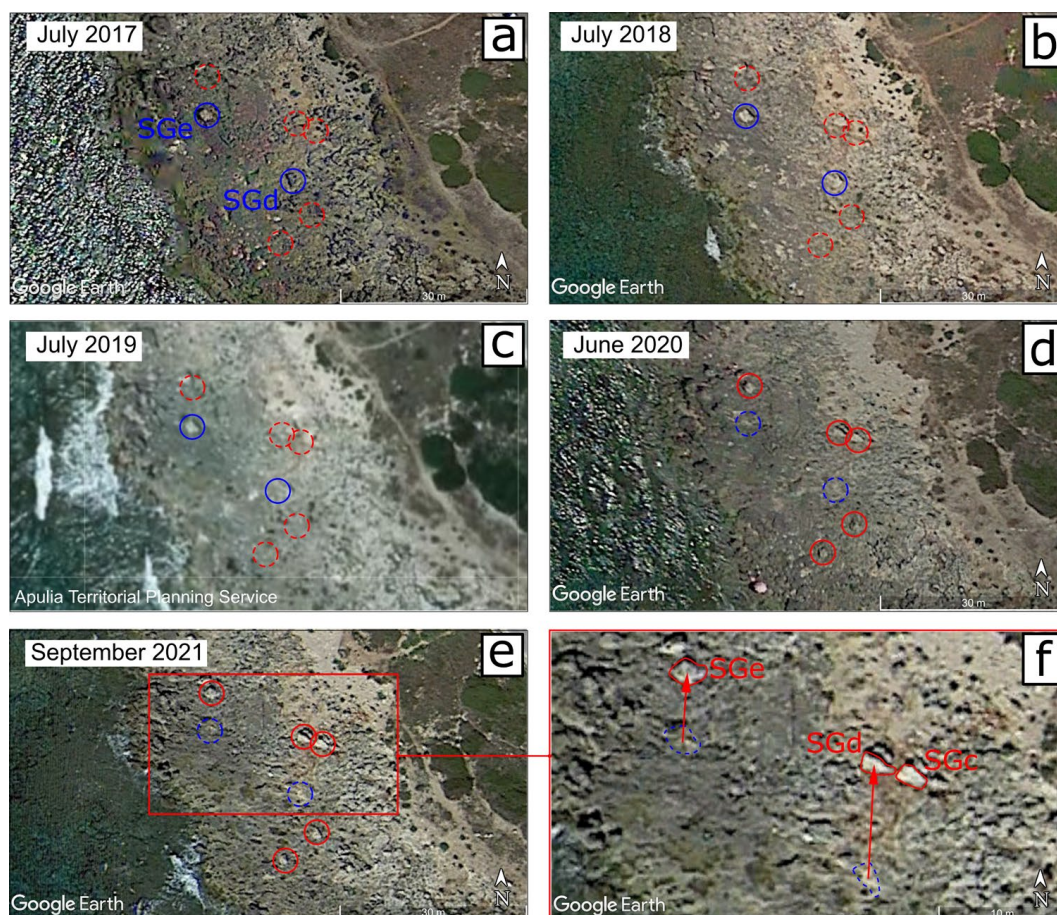


**Figure 5.** Torre San Giovanni coast ( $39^{\circ}54'03.59''$ – $39^{\circ}54'05.11''$  N,  $18^{\circ}05'06.89''$ – $18^{\circ}05'10.90''$  E) detection of boulder displacements: (a,b,d,e) GE images, eye elevation of 85 m; (c) regional aerial image; (f) transport vectors of SCd and SGe boulders, eye elevation of 41 m. Blue symbols, pre-displacement position; red symbols, post-displacement position. Dotted lines help the comparison.

### 3.2. Checking Previously Detected Displacement

The multi-temporal investigation was performed on the 81 displaced boulders previously detected by bi-temporal images analysis [9] with the aim to detect their annual mobility for the 4 years considered herein (see Sections 1 and 2). In what follows, some features of the boulder displacement are given with reference to the sites of Punta Prosciutto, Torre Suda, Mancaversa, and Punta Pizzo (see Figure 1).

Eighteen boulders that changed position between July 2018 and June 2020 were previously recognized along the Punta Prosciutto headland [9]. By means of the new analysis, it was found that all 18 boulders changed position between July 2019 and June 2020. For 13 boulders, both the initial and final positions were established; thus, the TD was determined (Table A10). Several changes in positions are shown in Figure 6. The case of the cluster composed of the PRi, PRj, PRk, and PRl boulders is particularly enlightening. Before the displacement, they were some meters to the southwest and differently arranged in comparison with the post-displacement arrangement (Figure 6f). One SSW–NNE transport

vector of about 5 m is drawn in the figure; actually, each of the boulders was transported from about 4 to 6 m. The boulder PRk is now vertically positioned; thus, it shows middle and minor axes in remote sensing images. The other three boulders of the cluster lie inclined on the coastal platform.

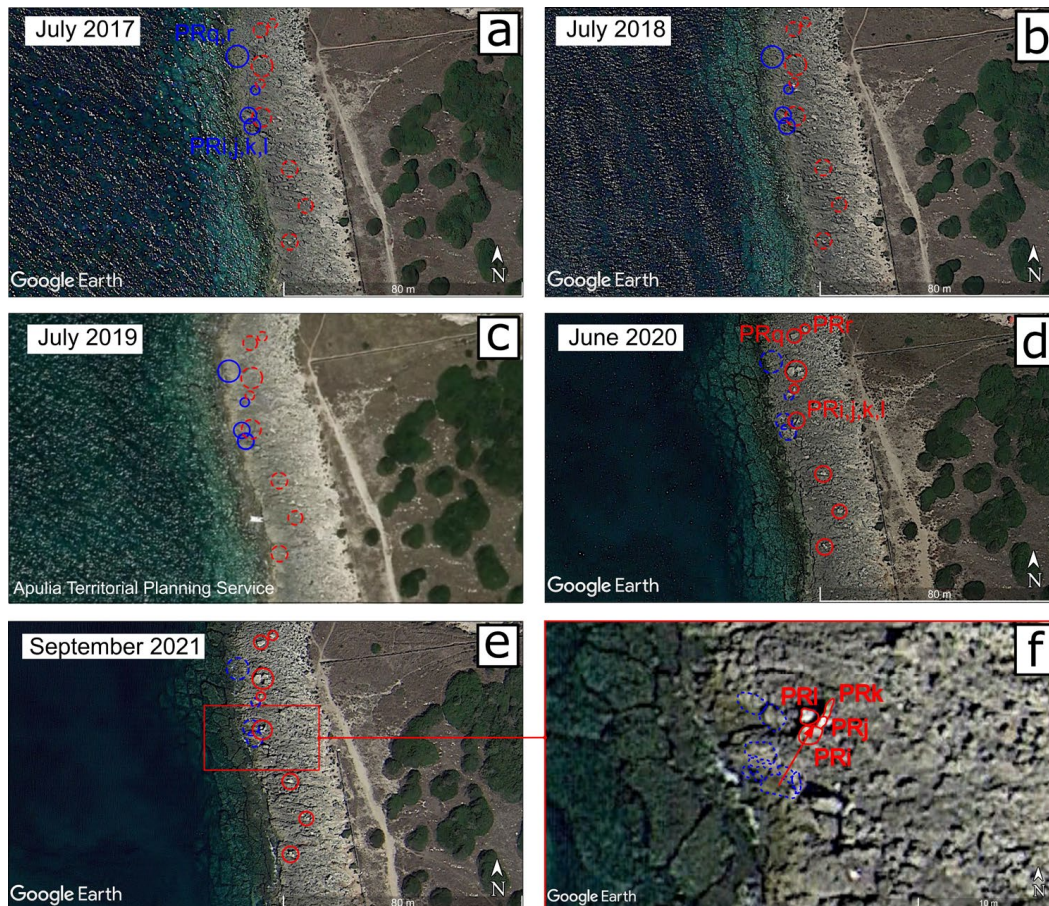


**Figure 6.** Punta Prosciutto headland ( $40^{\circ}17'32.93''$ – $40^{\circ}17'35.96''$  N,  $17^{\circ}45'41.75''$ – $17^{\circ}45'49.46''$  E) detection of boulder displacements: (a,b,d,e) GE images, eye elevation of 167 m; (c) regional aerial image; (f) transport vector of the PRi, j, k, l cluster, eye elevation of 35 m. Blue symbols, pre-displacement position; red symbols, post-displacement position. Dotted lines help the comparison.

The boulders PRq and PRr appear to be the result of the breaking of a singular boulder that likely occurred during transport (Figure 6a–c). Again, this geomorphological process took place between July 2019 and July 2020 (Figure 6c,d). Moreover, PRr was overturned between July 2020 and September 2021, thus changing position again (Figure 6d,e).

The largest displaced boulder detected by Delle Rose et al. [9] (named SUa) was found at Torre Suda (Figure 1). The size of this boulder is  $5.4 \times 4.6 \times 1.9$  m; it was displaced by about 9 m from SSE to NNW (Figure 7). Due to its middle axis dimension, SUa belongs to the class of fine blocks. It apparently slid and rotated about  $180^{\circ}$  over a submarine terrace plain just below the sea level, constrained in moving from the low cliff from which it was detached (Figure 7f). This constraint could have caused such an anomalous displacement (see also Figure A7 in Appendix A). SUa is placed in the initial position in the July 2017 to July 2019 images (Figure 7a–c), while its socket is not distinguishable both in the June 2020 and September 2021 images because it is close to the sea level.

By multi-temporal analysis, it was found that the 14 displacements detected at Torre Suda [9] evidently occurred between July 2019 and June 2020, although one of the displaced boulders (the SUi boulder; see Appendix A) had already undergone a first position change between July 2018 and July 2019.

Apart from SUa, another nine boulders detected by [9] have middle axes that exceed 2 m in length (very coarse boulders), including the MAa boulder (that was detected at Mancaversa site; Figure 1). Due to an unfavorable sun–object–sensor geometry, MAa is barely detectable in the July 2018 image. (Its presence can be deduced from the narrow shadow cast that marks its NE side; see Figure 8b.) Differently, in both the July 2017 and July 2019 images, the planar shape of MAa is well defined by topographic shadow. This boulder was moved between July 2019 and June 2020 (Figure 8c,d). It was detached from the parent rock and lifted and rotated due to the impact of an overtopping wave (Appendix A; Figures 8f and A7).

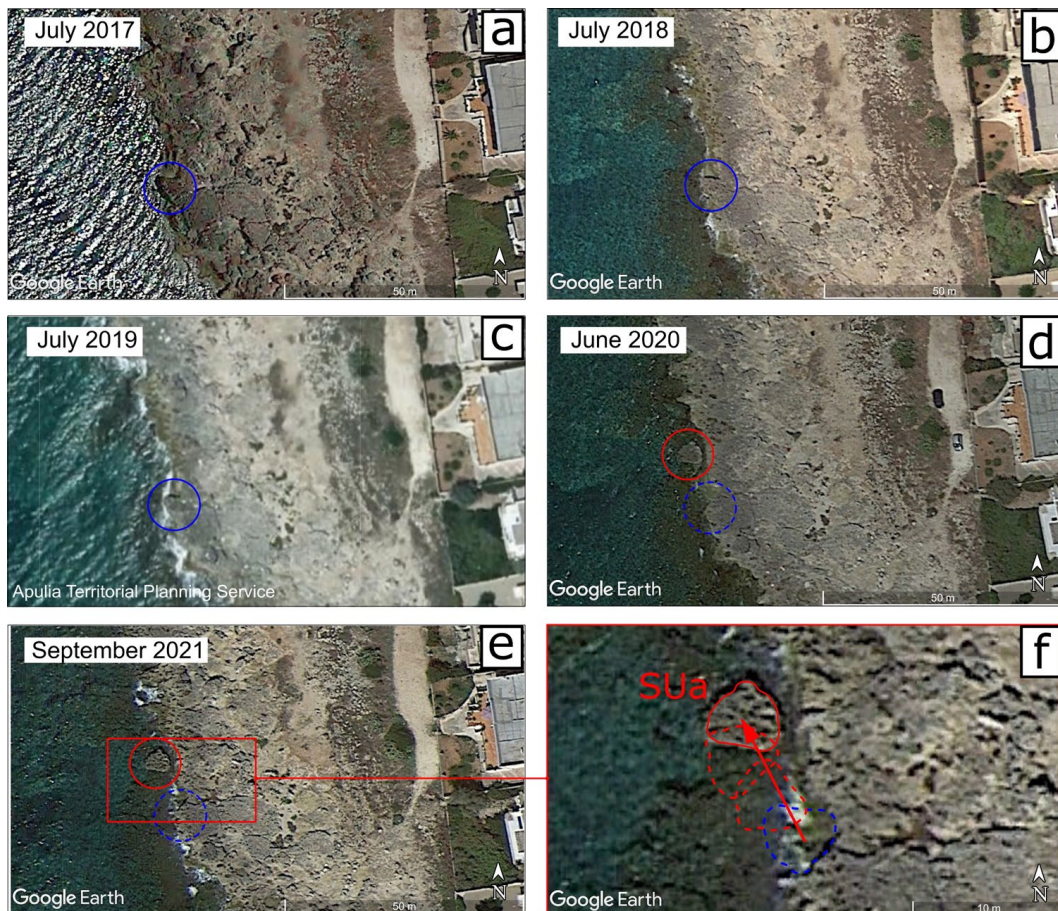


**Figure 7.** Torre Suda coast ( $39^{\circ}57'05.72''$ – $39^{\circ}57'07.66''$  N,  $18^{\circ}01'44.75''$ – $18^{\circ}01'49.31''$  E) detection of boulder displacements: (a,b,d,e) GE images, eye elevation of 99 m; (c) regional aerial image; (f) transport vector of SUa boulder, eye elevation of 35 m. Blue symbols, pre-displacement position; red symbols, post-displacement position. Dotted lines help the comparison.

Different from the cluster composed of the PRi, PRj, PRk, and PRl boulders (see above), other clusters were found with few changes in mutual spatial arrangement of the boulders after displacement. The case of the cluster composed of the PIa, PIb, PIc, PId, and PIE boulders is considered below (Figure 9). This cluster appears evenly moved by about 5 m from SSW to NNE (Figure 9f). Apparently, no collision between the boulders occurred. The 18 displacements found at Punta Pizzo [9] occurred between July 2019 and June 2020, as detected in the multi-temporal images.

In conclusion, by checking the displacements detected by [9], it was found that all the 81 boulders were moved between July 2019 and June 2020. Moreover, 1 of these 81 boulders had already undergone a first position change between July 2018 and July 2019, while another changed position yet again between June 2020 and September 2021.

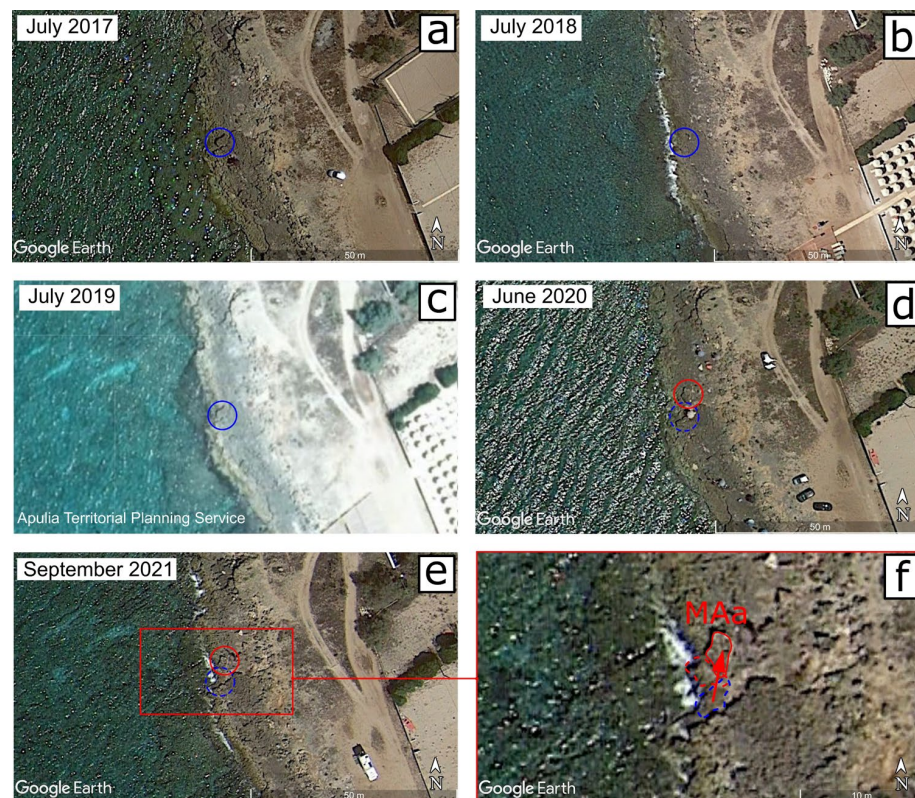


**Figure 8.** Mancaversa coast ( $39^{\circ}58'19.56''$ – $39^{\circ}58'21.50''$  N,  $18^{\circ}00'41.53''$ – $18^{\circ}00'46.09''$  E) detection of boulder displacements: (a,b,d,e) GE images, eye elevation of 99 m; (c) regional aerial image; (f) transport vector of MAA boulder, eye elevation of 37 m. Blue symbols, pre-displacement position; red symbols, post-displacement position. Dotted lines help the comparison.

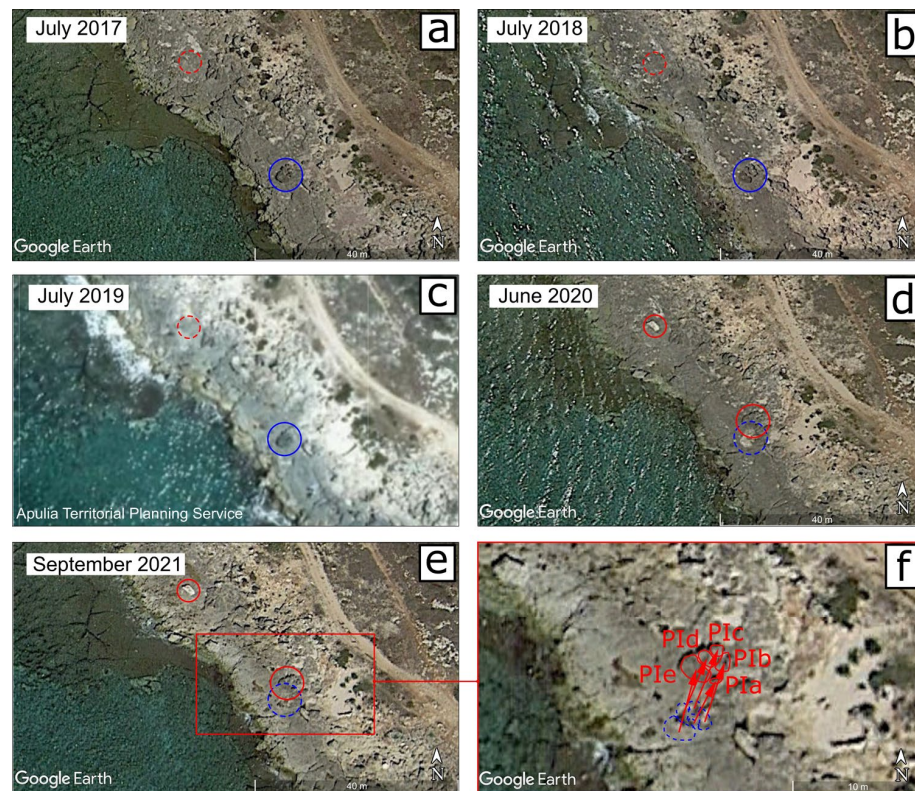


**Figure 9.** Punta Pizzo coast ( $39^{\circ}59'33.92''$ – $39^{\circ}59'35.48''$  N,  $17^{\circ}59'45.88''$ – $17^{\circ}59'49.52''$  E) detection of

boulder displacements: (a,b,d,e) GE images, eye elevation of 80 m; (c) regional aerial image; (f) transport vectors of Pla, b, c, d, e boulders, eye elevation of 35 m. Blue symbols, pre-displacement position; red symbols, post-displacement position. Dotted lines help the comparison.

### 3.3. Marine Weather Conditions and Severe Storms

The main features of the storms that could have caused the detected boulder displacements are reported in Table 2. All the identified storms (see Section 2.3 and Appendix B for the methodological approach) occurred during the CW seasons. Marine conditions with sea state 5 occurred in 4 days of the 2017–2018 CW season. The 2018–2019 CW season has been characterized by only two severe storms (including Vaia), both with sea state 6. Four storms with sea state from 5 to 7 (the highest value belonging to Detlef) hit the study area during the 2019–2020 CW season, which therefore was the stormiest period of the considered 4 years. Finally, two storms, both with sea state 6, occurred during the 2020–2021 CW season.

**Table 2.** Main features of the storms inferred using the GLOBO-BOLAM-MOLOCH model cascade. *R*, duration; *F*, fetch length; *U*, wind speed; *H*<sub>0</sub>, characteristic wave height. Sea state (degree, description) according to the Douglas sea scale.

Days	R (h)	F (km)	U (m/s)	H <sub>0</sub> (m)	Sea State
6 November 2017	12	600	14–16	3.4	5, rough
14 November 2017	12	800	16–18	4.0	5, rough
29 November 2017	15	900	14–16	3.9	5, rough
17 March 2018	12	700	16–18	4.0	5, rough
28–29 October 2018 <sup>1</sup>	48	700	12–14	5.7	6, very rough
2–3 February 2019	12	800	18–20	4.6	6, very rough
12–13 November 2019 <sup>2</sup>	24	900	20–22	8.8	7, high
24 November 2019	12	800	18–20	4.6	6, very rough
22 December 2019	24	400	14–16	4.7	6, very rough
2 March 2020	12	600	12–14	3.4	5, rough
3 December 2020	18	600	16–18	5.4	6, very rough
28–29 December 2020	12	600	18–20	4.6	6, very rough

<sup>1</sup> storm Vaia; <sup>2</sup> storm Detlef.

The *H*<sub>0</sub> associated with sea state 7 (storm Detlef) is 8.8 m. It is significantly larger than those associated with lower sea states, including the one of storm Vaia (5.7 m). Except for these two meteorological events, no other storms are associated with *H*<sub>0</sub> greater than 4.7 m (Table 2).

The nearshore wind conditions during the storms that occurred in the 2019–2020 CW season can be inferred from two out of the three wind gauge stations placed along the eastern coast of the Gulf of Taranto (Figure 1). Unfortunately, the Gallipoli station was not operational during this period (see Appendix B). The data extracted from the datasets of the Santa Maria di Leuca and Porto Cesareo stations are reported in Appendix C. They confirm that stronger wind conditions occurred during storm Detlef in comparison with the ones that occurred during the other storms of the 2019–2020 CW season. During 12–13 November 2019, the wind speed at 30 min averages measured at the Santa Maria di Leuca station ranged between 15 and 18 m/s for about 24 h, with a peak value of 24 m/s. The wind speed and duration during other storms were lower (Table A11). The measurements of the Porto Cesareo station confirm the above. The wind speed was around 20 m/s for almost the first half of November 13, while only during December 22 did it exceed 15 m/s for about 4 h (Figures A10–A13 in Appendix C).

## 4. Discussion

The following issues are discussed below: the annual mobility of the large clasts (Section 4.1), the cause of the massive displacement phenomenon (Section 4.2), and the marine weather conditions (Section 4.3). Complementary arguments are in Appendices C and D.

### 4.1. Annual Mobility of the Coastal Boulders

Along the eastern coast of the Gulf of Taranto, one hundred and nineteen boulders that changed position between July 2017 and September 2021 were detected by remote sensing image analysis (Sections 3.1 and 3.2). Moreover, two boulders (SUi and PRr) were apparently moved twice during this lapse of time. No boulder was displaced between July 2017 and July 2018. One boulder (SUi) was certainly displaced between July 2018 and July 2019. One hundred and eighteen displacements (including the second transport of the SUi boulder) occurred between July 2019 and June 2020 (Table 3). The PRr boulder experienced its second displacement between June 2020 and September 2021, which is the same interval of the change in position of ROI boulder.

**Table 3.** Annual intervals in which the detected displacements occurred.

		CW Season	No. of Displacements
1	July 2017–July 2018	2017–2018	0
2	July 2018–July 2019	2018–2019	1
3	July 2019–June 2020	2019–2020	118
4	June 2020–September 2021	2020–2021	2

The above result allows us to better define the period in which the massive displacement phenomenon recognized in the previous work [9] occurred, which is now limited to the interval 3 of Table 3. Moreover, storm Vaia must be ruled out as a possible causal storm.

Although some coastal boulders can be moved under rough sea conditions due to favorable combinations of hydrodynamic processes [57,58], the landward displacement of a high number of large boulders is typical of high-energy processes like tsunamis or exceptional storms [7,54,56]. During July 2017–September 2021, a western Mediterranean earthquake caused very small waves in the Gulf of Taranto unable to determine boulder displacements [9,59]. Consequently, the cause of the massive boulder displacement that occurred during the interval 3 (Table 3) must be found among the four storms that occurred during the 2019–2020 CW season (Table 2).

### 4.2. Event Responsible for the Massive Displacement

To relate the findings of the present study to those of ref. [9], the values of calculated wave height  $H$  at the initial position  $x_i$  (obtained from  $H_0$  considering the inland decay in height [60,61]; see Appendix B) were compared to the minimum wave height  $H_m$  required to move the SA boulders (Figure 10). This graph has been used by some authors to identify the causal events of different boulder deposits [2,50]. The hydrodynamic equations to calculate  $H$  and  $H_m$  are reported in Appendix B.

A value of  $H_s = 1.5$  m was taken as representative of the average rising of the sea level (storm surge + tide) during storm Detlef; for the weaker storms that occurred during the 2019–2020 CW season (Tables 2 and 3), a value of  $H_s = 0.5$  m was considered (see ref. [9] for details). In Figure 10, both the circles (boulders investigated in the present study) and squares (boulders investigated by [9]) form a trend that agrees with the line shape.  $H_m$  exceeds the height of the bore only for a few boulders. This graph suggests, again, that both storm Detlef was the cause of the massive displacement, and some boulders could be moved even during the weaker storms of the interval 3 (see Appendix D for more inferences). Most of the obtained TDs are few meters, while only a small percentage of boulders were moved beyond 10 m (Appendix A, Figure A7).

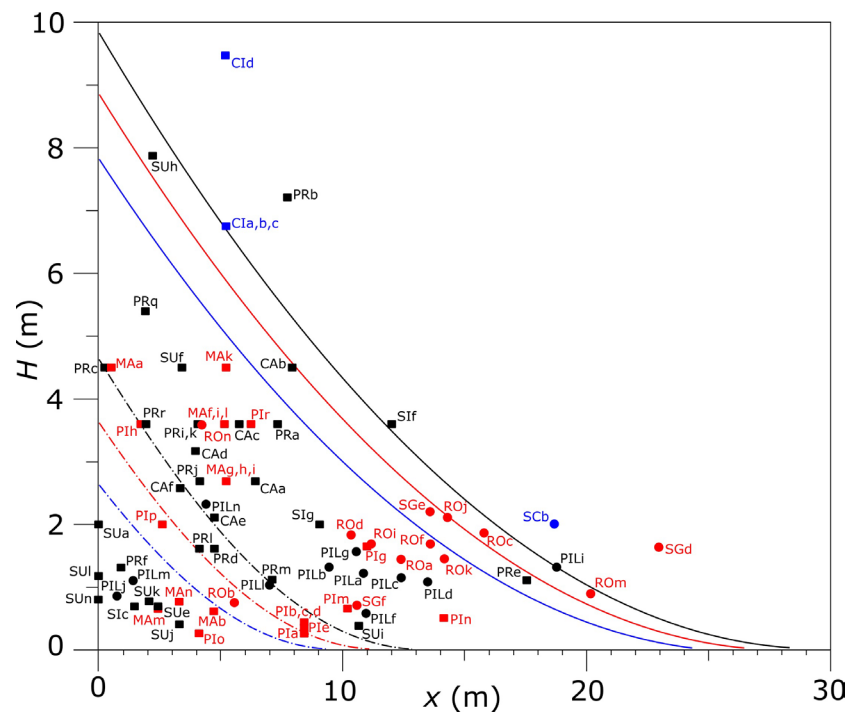


**Figure 10.** Comparison between wave height required to move the boulders  $H_m$  (circles and squares) and the height of the land-crossing bore  $H$  (lines) as a function of the distance  $x$  from the cliff edge and the coast height  $H_c$  (colors) for different characteristic wave height  $H_0$ . Continuous line: wave height for storm Detlef  $H_0 = 8.8$  m, and a total sea level increase (storm surge + tide)  $H_s = 1.5$  m (see text). Dot-dashed line: wave height for  $H_0 = 4.7$  m and  $H_s = 0.5$  m. Black,  $H_c = 0.5$  m; red,  $H_c = 1.5$  m; blue,  $H_c = 2.5$  m; circles: boulders investigated in the present study; squares: boulders investigated in the previous study [9].

The next research target is to compute the wave characteristics approaching the nearshore, for the case herein investigated, using the open-source SWAN (Simulating Waves Nearshore) code. However, the data collected and processed so far support that exceptional nearshore wave conditions drove the massive displacement phenomenon caused by storm Detlef along the eastern side of the Gulf of Taranto (see also Section 4.3). On the other hand, by on-site investigations performed after storm Detlef, 6 and 11 displaced boulders were found at Torre Suda (Sui second displacement, SUj, SUk, SUI, SUM, and SUN) and Sant’Isidoro (Sic, Sif, SIg, and eight additional boulders that were not detected by remote sensing imagery analysis because of their small size or short displacement), respectively [4,17,20,21] (Figure 1 for sites’ location). After storm Vaia, instead, only one case of boulder displacement at the Torre Suda site was detected (SUi, first displacement; see Figure A8a,b in Appendix A), while no displacements were found at the Sant’Isidoro site. Other evidence supporting the recognition of storm Detlef as the cause of the massive displacement can be found in Appendix D.

### 4.3. Marine Weather Conditions

The 12–13 November storm attracted the interest of several weather bureaus. It was named “Detlef” by the Meteorological Institute of Berlin Free University [62], and the name was adopted in some studies [4,63,64] (in [17], storm Detlef is provisionally named “Ionics19”). It was also named “Trudy” and “Bernardo” by the U.S. National Aeronautics and Space Administration and the Spanish Meteorological Agency, respectively [65–67]. On 10 November, a wide trough elongated from Northern Europe toward the western Mediterranean, creating a center of low atmosphere pressure. The cyclone transformed into a subtropical storm by 0600 UTC on 11 November [68] and then moved eastward over the central Mediterranean. Later, it reached the northern Adriatic Sea, causing an exceptional

sea level height in the Venice Lagoon [16,69,70]. Regarding the effects of storm Detlef on the study area, it must be noted that a strong wind over the eastern side of the Gulf of Taranto started soon after midnight on 12 November from the southeast and persisted for 24 h from almost the same direction, with an offshore fetch of about 900 km and an average wind speed of 20–22 m/s. The calculated characteristic wave height is 8.8 m (Table 2), which is greater than the maximum significant wave for a 100-year return period (Section 2).

A similar synoptic condition caused the 24 November storm with a weaker depression in the middle atmosphere. Again, the strongest winds blew from the south-eastern direction over the southern Apulia coast, with an intensity of 18–20 m/s (Table 2). In this case, the fetch was of about 800 km, while the duration of these conditions of about 12 h. Both the 22 December 2019 and the 2 March 2020 storms were caused by two middle-atmosphere lows coming from the north-eastern direction with respect to the Italian peninsula [9]. This difference caused a different impact over the study area, with more variability of the wind speed and direction. In the case of December 2019, the prevailing direction was from the western direction over the southern Apulia coast, with a shorter fetch because of the geographic shape of the Gulf of Taranto (Figure 1). The BOLAM model shows a wind of about 14–16 m/s at 10 m over the sea, associated with a duration of 24 h and a fetch of about 400 km. In the case of March 2020, the strongest wind blew from the south, with a lower intensity of about 12–14 m/s, a duration of 12 h, and a fetch of about 600 km. The calculated characteristic wave height for the storms that occurred between 24 November 2019 and 2 March 2020 ranges from 3.4 to 4.7 m (Table 2), values lower than that of the maximum significant wave for a 50-year return period (Section 2).

## 5. Conclusions

Exploring the 2017–2021 boulder mobility along the eastern coast of the Gulf of Taranto, a large interannual variability was found. A massive displacement occurred between 2019 fall and 2020 summer (involving at least 118 large clasts), while only 0–2 displacements occurred during each of the other explored years.

The cause of such a phenomenon must be found among the storms that occurred during the 2019–2020 CW season. Thus, differently from the previous statement [9], storm Vaia (28–29 October 2018) must be rejected as a possible causative storm. Considering several geomorphological, meteorological, and hydrodynamic evidences, storm Detlef (12–13 November 2019) is recognized as the causal event. In any case, it cannot be ruled out that the other storms of the 2019–2020 CW season could have moved some boulders.

For storm Detlef, the calculated characteristic wave height was just under 9 m, greater than the maximum significant wave for a 100-year return period. Differently, the characteristic wave heights for the other storms of the 2019–2020 CW season ranged from 3.4 to 4.7 m, values lower than the maximum significant wave for a 50-year return period. It must be highlighted that, along the studied coast, storm Vaia caused the displacement of only one boulder among those detected by the remote sensing analysis and the geomorphological survey.

This study expands the geomorphological dataset and deepens the marine weather knowledge on the massive displacement phenomenon identified by [9]. Such a phenomenon is the largest (for the number of boulders involved and length of the affected coast) among those that have occurred (and documented) in the Mediterranean Sea (see ref. [4]). This result confirms that overtopping flows due to storm waves can leave a significant geomorphological signature in coastal boulder deposits.

**Funding:** This research received no external funding.

**Data Availability Statement:** Data supporting the reported results can be found at the following links: <https://protezionecivile.puglia.it/annali-e-dati-idrologici-elaborati> (accessed on 10 September 2023), for the hydrological annals; <http://www.isac.cnr.it/dinamica/projects/forecasts/index.html> (accessed on 10 September 2023), for wind and wave data; <http://93.51.158.171/web/simop/home> (accessed on 10 September 2023), for wind data. Google Earth accessed on 28 January 2024.

**Acknowledgments:** The author thanks Gianluca Pappaccogli for the assistance in the processing of the remote sensing images; Paolo Martano for the calculation of the characteristic wave height and the description of the marine conditions; Luca Marzo, Luca Orlanducci, and Anna Lisa Signore for the assistance during the geomorphological surveys; and two anonymous reviewers for constructive comments on an earlier version of this work. The elaboration of remote sensing images (Figures 2–9) was carried out in the free open-source Inkscape editor.

**Conflicts of Interest:** The author declares no conflicts of interest.

## Appendix A

The data of the detected displaced boulders retrieved from remote sensing resources (see Sections 2 and 3) together with morphometric features determined by on-site investigation are reported below (Tables A1–A8). Geographical coordinates and TD were taken from the September 2021 GE image. In the course of the field survey, the inclination to the horizontal position of the boulders  $I$  and the dimensions of their axes ( $a_f$ , major;  $b_f$ , middle;  $c_f$ , minor) were measured and the lithology (Li) of the boulders (which, in turn, allows us to determine  $\rho_s$ ) established.

The PTS refers to some physical conditions (scenario) of the boulder before the displacement. The boulder can be isolated (sub-aerial, SA, or submerged, SB), laterally limited by joints (joint-bounded, JB), or located at the cliff edge (CE) [1,71]. These scenarios determine the possible three MTs (saltation/lifting, sliding, and overturning/rolling) during boulder displacement. SA and SB boulders can be lifted, slid, or rolled by the water flow; due to the movement constraints, JB boulders can only be lifted, while CE boulders can be lifted or rolled [54,56].

Figure A1 shows the socket left on the parent rock by the SCa boulder (Section 3.1). The socket was ephemeral, so that a few years after its formation, it has become almost indistinguishable from its rock parent (Figure A1a,b). The pre-transport setting of this boulder is “cliff edge” (CE) (see ref. [56]). All the other boulder detected in the present work are “sub-aerial” (SA) or “submerged” (SB) (see Tables A2, A4, A6 and A8).

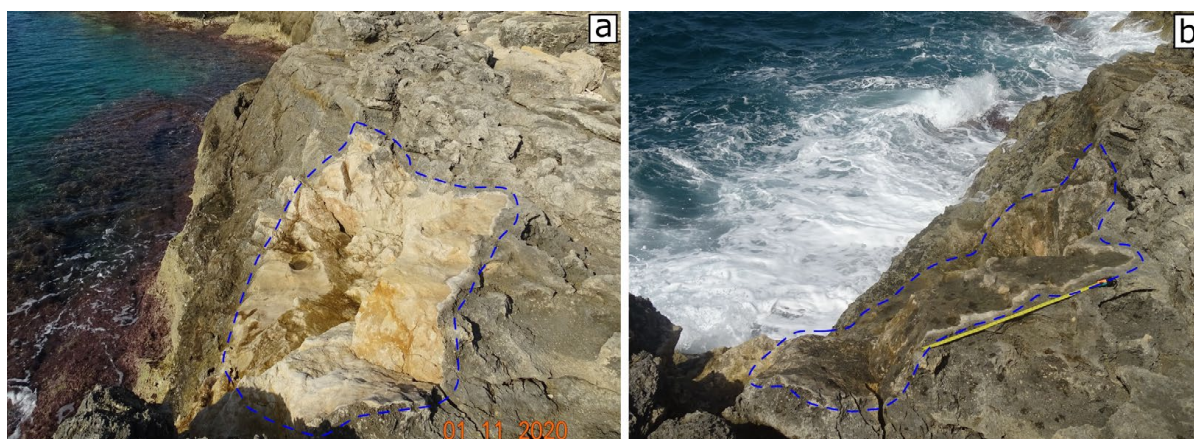


**Figure A1.** Santa Caterina site; the socket left by the SCa boulder (2.5 m over the sea level); (a) after about 1 year from the detachment (the image was taken 1 November 2020), the rock surface is fresh and not weathered; (b) after about 4 years from the detachment (the image was taken 22 September 2023, with 1 m long tape measure for scale), the rock surface is almost indistinguishable from the parent rock (see Figure 2d,e).

The post-transport position of SCa is unknown (Table A1). It was not recognized from GE images or in the field, and probably, SCa fell into the sea after detaching from its initial position.

**Table A1.** Initial (pre-displacement) and final (post-displacement) geographical coordinates of the storm-displaced boulders at Santa Caterina coast; ind., indeterminable; A.I., annual interval in which the displacement occurred (see Table 3).

ID	Initial Position		Final Position		A.I.
	Latitude	Longitude	Latitude	Longitude	
SCa	40°08′17.09″ N	17°59′19.21″ E	ind.	ind.	3
SCb	40°08′18.36″ N	17°59′18.47″ E	40°08′19.03″ N	17°59′18.85″ E	3

Differently from the socket of SCa, due to the different distance to the coastal cliff (Table A2), the surface of the SCb boulder is still fresh and unaltered (Figure A2). Moreover, since SCb lies in a shrub vegetation area, it is easily recognizable in remote sensing images (Figure 2d,e).



**Figure A2.** Santa Caterina site; the SCb boulder after the displacement occurred between July 2019 and September 2020 (the image was taken 22 September 2023, with 1 m long tape measure for scale). The whitish surface of SCb is uncovered by lichen and therefore still easily detectable in the field as well as by remote sensing images (see Section 3.1).

**Table A2.** Main features of the storm-displaced boulders at Santa Caterina coast; major and middle axes measured on GE remote sensing imagery:  $a_r$  and  $b_r$  (in m); dimensions of the axes taken in the field:  $a_f$ ,  $b_f$ , and  $c_f$  (in m); inclination on the ground  $I$ ; initial distances from the coastline  $x_i$ ; final distances from the coastline  $x_f$  (in m). TD, transport distance (in m); Li, lithology: C, calcarenite, L, limestone; Sh, shape: O, oblate ( $b/a > 0.6$ ,  $c/b < 0.6$ ); E, equant ( $b/a > 0.6$ ,  $c/b > 0.6$ ); B, bladed ( $b/a < 0.6$ ,  $c/b < 0.6$ ); P, prolate ( $b/a < 0.6$ ,  $c/b > 0.6$ ). FI, flatness index; PTS, pre-transport setting: JB, joint-bounded; SA, sub-aerial; SB, submerged; CE, cliff edge. MT, movement type: ST, saltation; SL, sliding; OV, overturning. ind., indeterminable. Note: Abbreviations are the same for Tables A4, A6 and A8.

ID	$a_r$	$b_r$	$a_f$	$b_f$	$c_f$	$I$	$x_i$	$x_f$	TD	Li	Sh	FI	PTS	MT
SCa	3.3	1.2	-	-	-	-	0.8	ind.	-	C	-	-	CE	-
SCb	1.8	1.5	1.8	1.6	0.7	5°	18.8	21.6	15.4	C	O	2.5	SA	OV

**Table A3.** Initial (pre-displacement) and final (post-displacement) geographical coordinates of the storm-displaced boulders at the Pilella coast. Note: See caption of Table A1 for abbreviations.

ID	Initial Position		Final Position		A.I.
	Latitude	Longitude	Latitude	Longitude	
PILa	39°55′22.66″ N	18°03′35.76″ E	39°55′22.72″ N	18°03′35.80″ E	3
PILb	39°55′22.60″ N	18°03′35.42″ E	39°55′22.68″ N	18°03′35.51″ E	3
PILc	39°55′22.27″ N	18°03′34.62″ E	39°55′22.35″ N	18°03′34.66″ E	3
PILd	39°55′22.24″ N	18°03′34.49″ E	39°55′22.33″ N	18°03′34.50″ E	3
PILe	ind.	ind.	39°55′23.54″ N	18°03′32.43″ E	3
PILf	39°55′23.83″ N	18°03′31.60″ E	39°55′23.88″ N	18°03′31.63″ E	3
PILg	39°55′23.97″ N	18°03′31.61″ E	39°55′24.11″ N	18°03′31.72″ E	3
PILh	ind.	ind.	39°55′24.08″ N	18°03′30.58″ E	3
PILi	39°55′24.39″ N	18°03′31.08″ E	39°55′24.49″ N	18°03′31.12″ E	3
PILj	39°55′25.09″ N	18°03′27.70″ E	39°55′25.10″ N	18°03′27.78″ E	3
PILk	39°55′25.38″ N	18°03′27.86″ E	ind.	ind.	3
PILl	39°55′26.41″ N	18°03′27.20″ E	39°55′26.49″ N	18°03′27.26″ E	3
PILm	39°55′26.86″ N	18°03′26.56″ E	39°55′26.96″ N	18°03′26.64″ E	3
PILn	39°55′27.29″ N	18°03′26.47″ E	39°55′27.32″ N	18°03′26.54″ E	3

Several displaced boulders show a high value of *I*. As an example, the PILn boulder (Figure A3) is inclined of about 55° with respect to the ground (Table A4). Such an arrangement can cause the underestimation of the horizontal dimensions of the boulders from remote sensing imagery (Section 3).

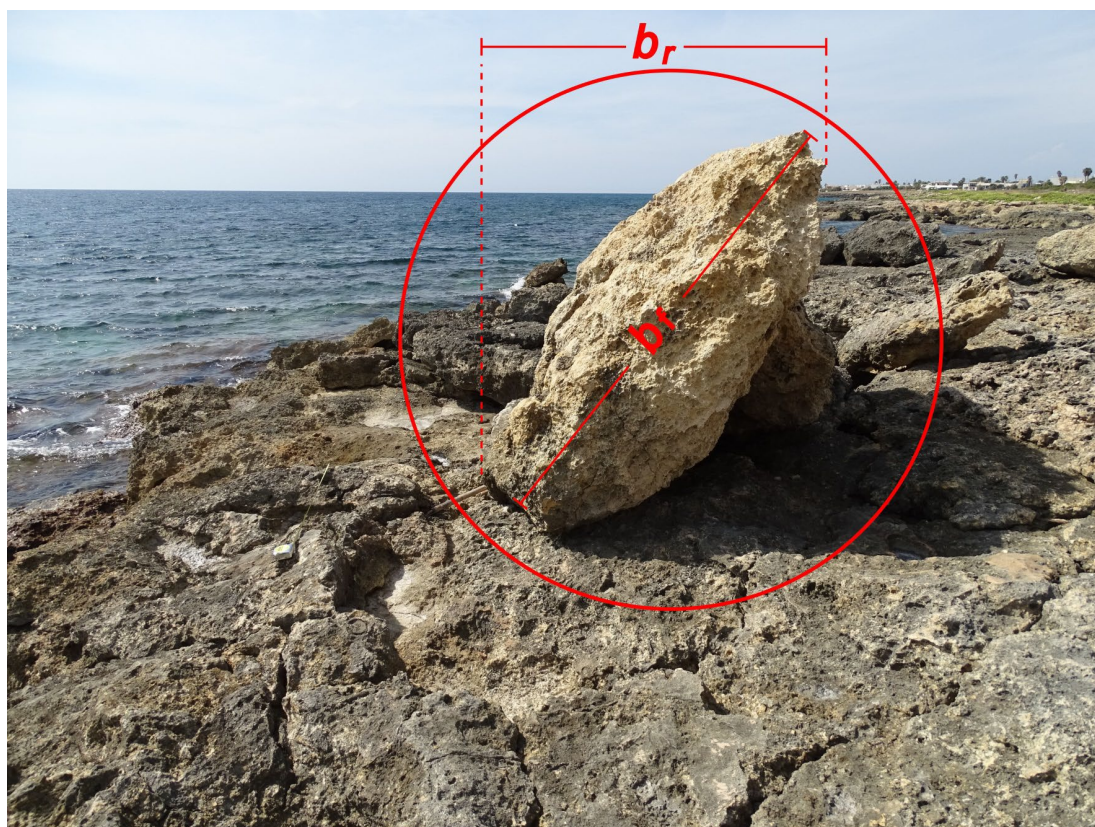


**Figure A3.** Pilella site; the PILn boulder lies on a smaller boulder and forms an angle of about 55° with respect to the ground. Note the difference in length between  $b_r$  and  $b_f$  (see the caption of Table A2 for symbols).

As mentioned in Section 2.3, after estimating the center point of the boulders at the initial and final positions, several TDs were verified onsite by means of a measuring tape. At the Pilella coast, the measurements taken almost never differed more than 5% from those detected in the remote sensing images (see also Appendix B in ref. [9]). As an example, for the PILm boulder, 3.4 m was measured in the field against 3.7 m in the image.

**Table A4.** Main features of the storm-displaced boulders at the Pilella coast. Note: See caption of Table A2 for abbreviations.

ID	$a_r$	$b_r$	$a_f$	$b_f$	$c_f$	$I$	$x_i$	$x_f$	TD	Li	Sh	FI	PTS	MT
PILa	1.6	0.9	1.6	1.0	0.5	0–5°	10.8	12.4	3.6	C	O	2.6	SA	OV
PILb	2.0	1.0	1.8	1.0	0.4	0–5°	9.4	10.5	4.1	C	B	3.5	SA	OV
PILc	1.5	1.0	1.5	0.9	0.4	~20°	12.4	14.7	2.5	C	B	3	SA	OV
PILd	2.0	1.2	1.9	1.0	0.6	0–5°	13.6	15.6	2.6	C	B	2.4	SA	OV
PILe	2.3	1.6	2.5	1.5	0.3	~15°	ind.	13.2	-	C	O	6.7	SB	ST,OV
PILf	2.2	1.5	2.4	1.2	0.5	~60°	10.9	12.5	1.5	C	B	3.6	SA	SL
PILg	1.7	1.4	1.5	1.3	0.6	~10°	10.6	15.5	4.8	C	O	2.3	SA	OV
PILh	2.2	1.0	1.9	1.0	0.5	5°	ind.	3.9	-	L	B	2.9	SB	ind.
PILi	1.9	1.1	2.2	1.1	0.4	5°	18.8	20.4	2.6	C	B	4.1	SA	ST,OV
PILj	3.1	1.9	3.0	1.8	0.6	5°	0.7	1.9	1.6	C	O	4	SB	SL
PILk	2.0	1.4	-	-	-	-	6.9	ind.	-	-	-	-	SA	-
PILl	2.0	1.1	2.1	1.1	0.8	0–5°	7.0	8.9	3.3	L	P	2	SA	OV
PILm	2.1	1.1	2.0	1.0	0.4	0–5°	1.1	3.7	3.2	C	B	3.7	SA	OV
PILn	2.2	1.2	2.1	1.8	0.4	~55°	4.4	6.2	1.9	C	O	4.9	SA	OV

Most of the boulders examined at Pilella clearly show fresh and not weathered surfaces, while the surfaces covered by lichen and with karst dissolution features are in contact with the ground. They must be considered as SA overturned boulders.

The initial position of both the PILe and PILh boulders was not detected in the time series remote sensing images (Table A4). At its final position, the upper surface of PILe is whitish and is covered by decaying marine plants (Figure A4a). This suggests that it was below sea level before the transport. PILh is currently just over the edge of the cliff, and it presents some solution pans over its upper surface (Figure A4b). Before the displacement, it was roughly at the sea level. For the PILf and PILj boulders, some tracks referable as drag marks were observed along their trajectory, and consequently, their type of movement is considered SL (Table A4). For the remaining boulders, no elements useful to define with good confidence the MT were identified.

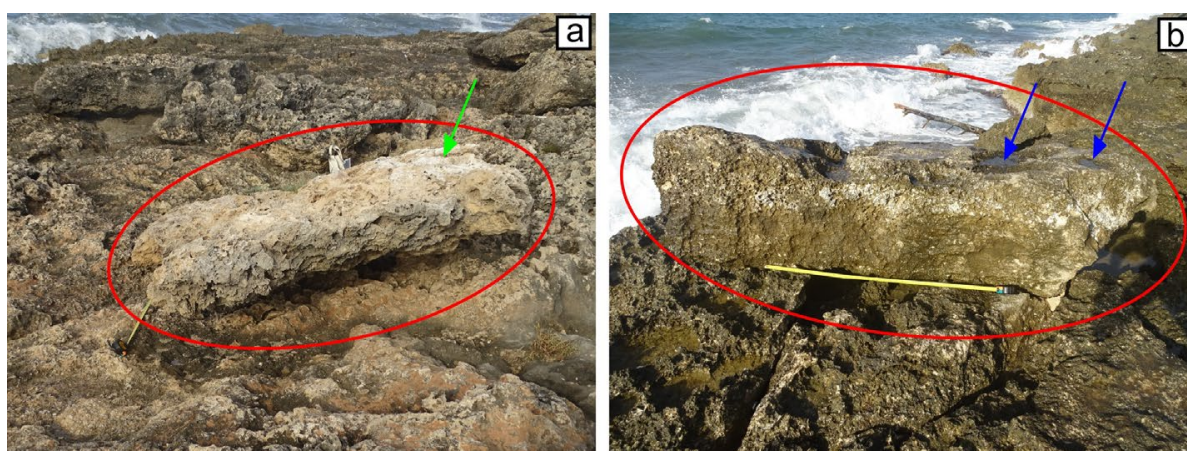


**Figure A4.** Pilella site; (a) the PILe boulder (green arrow indicates decaying marine plants); (b) the PILh boulder (blue arrows indicate solution pans).

**Table A5.** Initial (pre-displacement) and final (post-displacement) geographical coordinates of the storm-displaced boulders at the Posto Rosso coast. Note: See caption of Table A1 for abbreviations.

ID	Initial Position		Final Position		A.I.
	Latitude	Longitude	Latitude	Longitude	
ROa	30°54'45.53" N	18°04'20.88" E	30°54'47.70" N	18°04'20.99" E	3
ROb	30°54'46.19" N	18°04'20.51" E	30°54'46.21" N	18°04'20.55" E	3
ROc	30°54'46.87" N	18°04'20.58" E	30°54'46.90" N	18°04'20.69" E	3
ROd	30°54'47.88" N	18°04'18.76" E	30°54'48.03" N	18°04'18.79" E	3
ROe	ind.	ind.	30°54'48.30" N	18°04'17.88" E	3
ROf	30°54'48.40" N	18°04'17.90" E	30°54'48.45" N	18°04'17.96" E	3
ROg	ind.	ind.	30°54'48.39" N	18°04'17.57" E	3
ROh	ind.	ind.	30°54'48.43" N	18°04'17.54" E	3
ROi	30°54'48.38" N	18°04'17.34" E	30°54'48.44" N	18°04'17.36" E	3
ROj	30°54'48.40" N	18°04'17.44" E	30°54'48.51" N	18°04'17.47" E	3
ROk	30°54'48.45" N	18°04'17.59" E	30°54'48.52" N	18°04'17.37" E	3
ROl	ind.	ind.	30°54'48.79" N	18°04'17.15" E	4
ROm	30°54'49.29" N	18°04'16.85" E	30°54'49.40" N	18°04'16.95" E	3
ROn	30°54'49.02" N	18°04'15.97" E	30°54'48.48" N	18°04'16.41" E	3
ROo	ind.	ind.	30°54'49.68" N	18°04'16.38" E	3
ROp	ind.	ind.	30°54'49.71" N	18°04'16.43" E	3

Many coarse boulders were detected at the Posto Rosso site (Section 3.1, Table A6). The ROa boulder was detached and overturned (Figure A5a). The boulder ROI also appears to have been overturned (Figure A5b). The ROn boulder, despite its large size, was transported for 17.5 m due to the water flow (Figure A5c,d). This measure, taken using a measuring tape, differs from the one detected in the remote sensing image by less than 0.5 m (Table A6). In Figure A5c, one phase of estimating the position of the geometric center of the boulder before the movement can be observed. Again, ROn is not overturned, and no drag marks are observed over the platform surface. Thus, it appears to have undergone a saltation movement.

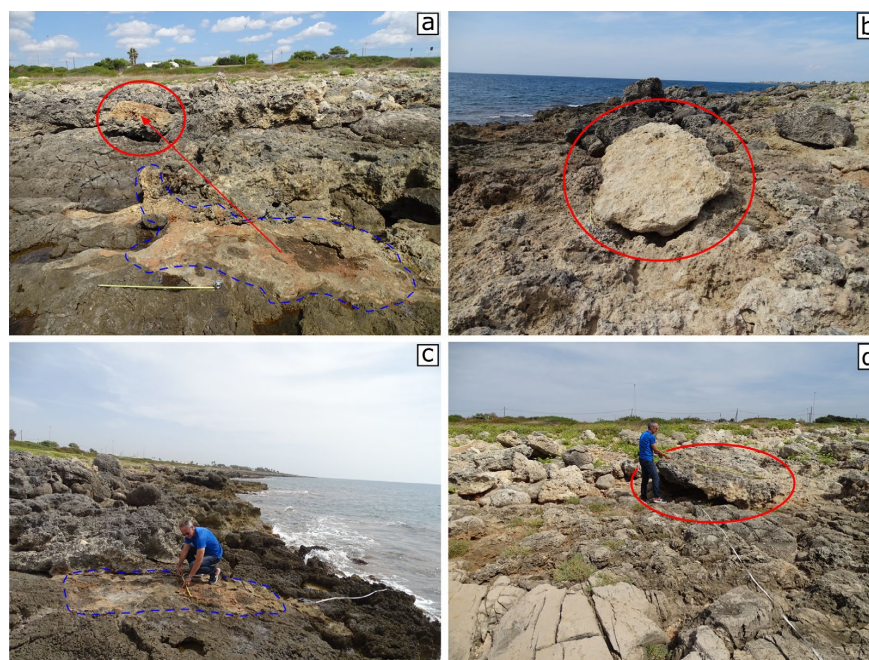


**Figure A5.** Posto Rosso site; (a) the overturned ROa boulder and (in the foreground) its socket (with 1 m long tape measure for scale); (b) the geomorphological arrangement of ROI boulder that was displaced during the 2020–2021 CW season (see Section 3.1); (c) the socket of the ROn boulder; (d) the ROn boulder was detached from its initial position and displaced 17–17.5 m inland (see text).

**Table A6.** Main features of the storm-displaced boulders at the Posto Rosso coast. Note: See caption of Table A2 for abbreviations.

ID	$a_r$	$b_r$	$a_f$	$b_f$	$c_f$	$I$	$x_i$	$x_f$	TD	Li	Sh	FI	PTS	MT
ROa	2.7	1.4	2.7	1.3	0.8	0–5°	12.3	18.5	5.8	C	P	2.5	SA	OV
ROb	2.8	1.3	2.9	1.4	0.6	0–5°	5.7	6.7	1.9	C	B	3.6	SA	SL
ROc	1.6	1.3	1.7	1.4	0.5	0–5°	15.9	18.2	2.5	C	O	3.1	SA	ST,OV
ROd	2.5	1.9	2.4	1.5	0.7	~20°	10.4	14.7	4.5	C	O	2.8	SA	OV
ROe	2.1	1.6	2.3	1.6	0.5	0–5°	ind.	11.2	-	C	O	3.9	SB	ind.
ROf	1.8	1.4	1.7	1.4	0.7	0–5°	13.6	15.8	2.1	C	O	2.2	SA	ST,OV
ROg	1.5	0.9	1.3	0.9	0.4	~25°	ind.	14.6	-	C	B	2.7	SB	ST
ROh	1.6	0.9	1.7	0.9	0.7	0–5°	ind.	14.4	-	C	P	1.8	SB	ST,OV
ROi	2.8	1.3	2.7	1.4	0.7	~10°	11.1	12.6	1.9	C	B	2.9	SA	ST,OV
ROj	2.6	1.5	2.4	1.7	0.8	~20°	14.4	16.7	3.1	C	B	2.6	SA	OV
ROk	1.7	1.2	1.7	1.3	0.7	~15°	14.2	16.1	2.1	C	O	2.1	SA	OV
ROl	1.8	1.3	1.9	1.2	0.3	~20°	ind.	9.3	-	C	O	5.2	SB	OV
ROm	1.5	0.8	1.4	0.8	0.5	0–5°	20.3	25.2	4.8	C	P	2.2	SA	ST,OV
ROn	3.1	1.8	2.8	2.1	0.5	~20°	4.2	20.7	17.1	C	O	4.9	SA	ST
ROo	1.3	0.9	1.4	0.9	0.5	~10°	ind.	25.3	-	C	B	2.3	SB	ST,OV
ROp	1.5	0.8	1.7	1.1	0.5	~25°	ind.	26.4	-	C	O	2.8	SB	ST,OV

**Table A7.** Initial (pre-displacement) and final (post-displacement) geographical coordinates of the storm-displaced boulders at the Torre San Giovanni coast. Note: See caption of Table A1 for abbreviations.

ID	Initial Position		Final Position		A.I.
	Latitude	Longitude	Latitude	Longitude	
SGa	ind.	ind.	39°54'03.86" N	18°05'09.25" E	3
SGb	ind.	ind.	39°54'03.99" N	18°05'09.47" E	3
SGc	ind.	ind.	39°54'04.46" N	18°05'09.50" E	3
SGd	39°54'04.18" N	18°05'09.34" E	39°54'04.49" N	18°05'09.38" E	3
SGe	39°54'04.52" N	18°05'08.72" E	39°54'04.73" N	18°05'08.76" E	3
SGf	39°54'05.57" N	18°05'08.45" E	39°54'05.61" N	18°05'08.53" E	3

Several of the displaced boulders are rather flat (e.g., PILE and SGd; see Tables A4 and A8, respectively). The flat SGd boulder (FI = 6; Figure A6) was transported almost 10 m from an initial position more than 20 m away from the coastline.

For the SGd, SGe, and SGf boulders, the TD was verified onsite. Again, these measures do not differ by more than 5% from those detected in the remote sensing images.



**Figure A6.** Torre San Giovanni site; SGc (in the foreground) and SGd boulders. As a result of the water flow transport, they formed two imbricated clusters together with other small boulders.

**Table A8.** Main features of the storm-displaced boulders at the Torre San Giovanni coast. Note: See caption of Table A2 for abbreviations.

ID	$a_r$	$b_r$	$a_f$	$b_f$	$c_f$	$I$	$x_i$	$x_f$	TD	Li	Sh	FI	PTS	MT
SGa	1.5	0.9	1.4	1.1	0.4	0–5°	ind.	14.9	-	C	O	3.1	SB	ST,OV
SGb	1.8	1.1	1.8	1.0	0.3	0–5°	ind.	22.3	-	C	B	4.7	SB	ST,OV
SGc	1.9	1.1	1.8	1.2	0.3	0–5°	ind.	31.4	-	C	O	5	SB	ST,OV
SGd	2.1	0.9	2.3	1.3	0.3	~45°	22.8	28.6	9.5	C	B	6	SA	ST,OV
SGe	2.4	1.7	2.2	1.7	0.7	0–5°	13.8	18.2	6.5	C	O	2.8	SA	ST,OV
SGf	1.6	0.8	1.5	1.2	0.6	~30°	10.4	11.7	2.4	C	O	2.2	SA	OV

When both the initial and final positions of the detected boulders were established, the transport distance was calculated (Sections 4.1 and 4.2). In Tables A9 and A10, a list of these 84 boulders is given.

**Table A9.** Displaced boulders detected in this study for which TD was calculated and whose position changed between July 2019 and June 2020.

Site	Boulder ID <sup>1</sup>
Santa Caterina	SCb
Pilella	PILa, PILb, PILc, PILd, PILf, PILg, PILi, PILj, PILl, PILm, PILn
Posto Rosso	ROa, ROb, ROc, ROd, ROf, ROi, ROj, ROk, ROm, ROn
Torre San Giovanni	SGd, SGe, SGf

<sup>1</sup> For geographical coordinates, transport distance, dimensions of the axes, pre- and post-displacement distances from the coastline, lithology, shape, flatness index, pre-displacement setting, and movement type, see Tables A1–A8.

**Table A10.** Displaced boulders detected by [9] whose position results changed between July 2019 and June 2020 and for which TD was calculated.

Site	Boulder ID <sup>1</sup>
Punta Prosciutto	PRa, PRb, PRc, PRd, PRe, PRf, PRi, PRj, PRk, PRL, PRm, PRq, PRr
Sant’Isidoro	SIf, SIg
Punta Pizzo	PIa, PIb, PIc, PId, PIe, PIg, PIh, PIj, PIk, PIn, PIo, PIp, PIr
Mancaversa	MAa, MAb, MAC, MAf, MAG, MAh, MAi, MAj, MAK, MAL, MAm, MAN
Torre Suda	SUa, SUe, SUf, SUh, SUi, SUj, SUk, SUL, SUN
Capilungo	CAa, CAb, CAc, CAd, CAe, CAf
Ciaro	Cla, Clb, Clc, Clid

<sup>1</sup> For geographical coordinates, transport distance, dimensions of the axes, pre- and post-displacement distances from the coastline, lithology, shape, flatness index, pre-displacement setting, and movement type, see Appendix A in ref. [9].

Based on the above sets of data, it can be deduced that more than 65% of medium-to-coarse boulders were moved less than 5 m, while less than 15% were moved more than 10 m, including the SCb and ROn boulders (Figure A7; Tables A1, A2, A5 and A6 for morphometric data). This result agrees with those of other studies performed with different methods on Mediterranean coasts [72,73].

As reported in Section 3, two boulders underwent two displacements during 2017–2021. In the case of the SUi boulder (Section 3.2), this singular mobility can be due to a slipway ramp that channels the water flows (Figure A8).

The PTS of the MAa boulder was considered as joint-bounded (JB) in the previous work [9]. It was detached from the parent rock along a vertical joint system, leaving a small step on the ground surface (Figure A9). In any case, MAa did not jump over the step, as it was moved in opposite direction. The boulder could therefore be considered SA. Since the slope angle ( $\theta$ ) is zero, the minimum wave height calculated by the Equations (A4) and (A7) (Appendix B) is the same ( $H_m = 4.5$  m; see Figure 10).

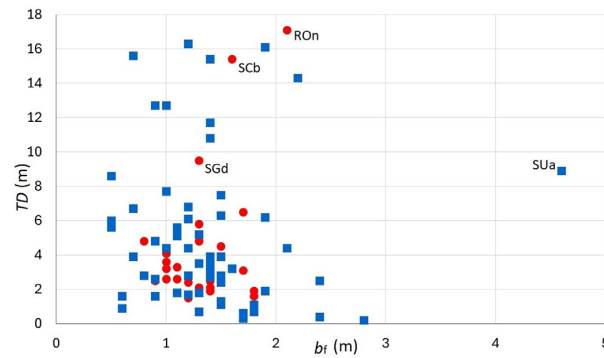


**Figure A7.** Transport distance (TD) vs. middle axis measured in the field ( $b_f$ ). Red circles, boulders detected in the present study; blue squares, boulders detected in the previous study [9].

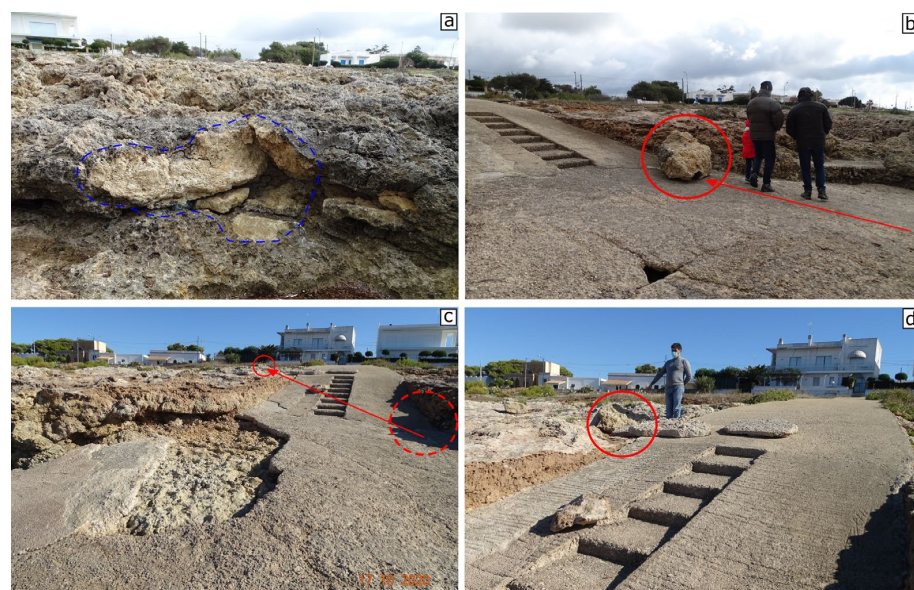


**Figure A8.** Torre Suda site; (a) the socket of the SUi boulder (image taken the 23 February 2019); (b) SUi boulder lying on a slipway ramp after the first movement (image taken 23 February 2019); (c,d) SUi boulder displaced from the ramp due to the second movement (images taken 17 October 2020).



**Figure A9.** Mancaversa site; the MAa boulder lying about 4.5 m from its initial position (in the foreground); rock joints are indicated by green arrows (see text).

For the MAa boulder, the TD was verified onsite. Again, this measure does not differ by more than 5% from that detected in the remote sensing image.

## Appendix B

As mentioned in Section 2.3, the windstorm characteristics (duration  $R$ , length of the fetch over the sea surface  $F$ , fetch direction  $D$ , and wind speed  $U$ ) determined by the forecast map archive of the BOLAM-MOLOCH model [53] were used to calculate the spectral peak wave height from the similarity relation equations [74,75]. They relate  $T$  (wave period),  $H_0$ , and  $R$  to the wind speed at 10 m height offshore  $U$  and to the fetch over the sea  $F$ :

$$gT/U = 0.286(gF/U^2)^{1/3}, \quad (A1)$$

$$gH_0/U^2 = 0.0016(gF/U^2)^{1/2}, \quad (A2)$$

$$gR/U = 68.8(gF/U^2)^{2/3}, \quad (A3)$$

where  $g$  is the gravity acceleration. This procedure has already been used in previous works [9].

The duration  $R$  of stability of wind conditions, estimated from the wind maps, was used as a limiting factor to calculate an effective fetch  $F$  for Equations (A1) and (A2) whenever the actual geometric fetch appears to be longer. It must be noted that  $H_0$  is nearly equivalent to the significant wave height [76,77].

Data of wind gauge stations placed along the coast (Figure 1) have been used to infer the nearshore wind conditions during storms presumed to be responsible for changes in boulder position. Due to the incompleteness and inhomogeneity of the datasets, these conditions can be only partially defined. The Santa Maria di Leuca and Gallipoli stations are managed by the Apulia Civil Protection that publishes comprehensive annual reports (named *Annali Idrologici*, Hydrological Annals) [78–82]. These report the daily average and maximum together with four 30 min averages at four selected hours of the day (00, 06, 12, and 18). However, the Gallipoli station has been in operation only since November 2020. The Porto Cesareo station belongs to the Apulia Meteomarine Network (*SIMOP*, *Sistema Informativo Meteo Oceanografico delle Coste Pugliesi*, in Italian); its data are publicly available online and consist of 15 min measures of wind speed and direction [83]. The Porto Cesareo station has been in operation since February 2019.

The displacement of boulders due to wave impact on the coast starts when the hydrodynamics forces exceed the resistance forces of net friction [54,55]. Nandasena et al. [1,71] and Nandasena [56] elaborated a set of equations to calculate the minimum wave height ( $H_m$ ) required to set in motion and cause onshore transport of the boulders, depending on PTS and MT. For SA and SB boulders moved by saltation/lifting, sliding, and rolling,  $H_m$  is as follows, respectively:

$$H_m = \frac{2c(\rho_s/\rho_w - 1)\cos\theta}{C_L}, \quad (A4)$$

$$H_m = \frac{2c(\rho_s/\rho_w - 1)(\mu\cos\theta + \sin\theta)}{C_D(c/b) + \mu C_L}, \quad (A5)$$

$$H_m = \frac{2c(\rho_s/\rho_w - 1)(\cos\theta + (c/b)\sin\theta)}{C_D(c^2/b^2) + C_L}, \quad (A6)$$

For JB boulders moved by saltation/lifting,  $H_m$  is as follows:

$$H_m = \frac{2c(\rho_s/\rho_w - 1)(\cos\theta + \mu\sin\theta)}{C_L}, \quad (A7)$$

For CE boulders moved by saltation/lifting and rolling,  $H_m$  is as follows, respectively:

$$H_m = \frac{2c(\rho_s/\rho_w - 1)}{C_L - \mu C_D(c/b)}, \tag{A8}$$

$$H_m = \frac{2c(\rho_s/\rho_w - 1)}{C_L - C_D(c^2/b^2)}, \tag{A9}$$

In the Equations (A4)–(A9):  $b$  = b-axis length (m);  $c$  = c-axis length (m);  $\rho_s$  = density of boulder ( $\text{kg m}^{-3}$ );  $\rho_w$  = density of seawater ( $\text{kg m}^{-3}$ );  $\theta$  = bed slope angle (degrees);  $\mu$  = coefficient of static friction along the ground surface;  $C_L$  = lift coefficient;  $C_D$  = drag coefficient. As is known, the values of the coefficients  $C_D$  and  $C_L$  are crucial in determining the reliability of the results [61,84,85]. Their correct determination would require considering the influence of environmental factors like the substrate roughness and flow turbulence and performing hydrodynamic site-specific measurements. Considering that, in the present work, the use of the above equations is simply aimed at a comparison with the results of the previous work [9], the values of 1.95 for  $C_D$ , 0.178 for  $C_L$ , and 0.7 for  $\mu$  were used (see, e.g., refs. [1,9,48,86,87]). Again, based on the local geology, the following values of density ( $\rho_s$ ) were used:  $1.8 \text{ kg m}^{-3}$  for calcarenite;  $2.2 \text{ kg m}^{-3}$  for limestone.

To estimate the decrease in wave height over the shore, say the effective wave height  $H$  impacting the boulder at the distance  $x$  from the shoreline, the equation of Cox and Machemehl [60] was used:

$$H = [(R + H_s - H_c)^{1/2} - 5x/(Tg^{1/2})]^2, \tag{A10}$$

In Equation (A10):  $x$  = distance from the coastline (m);  $g$  = gravity acceleration;  $T$  was estimated by Equation (A1); the breaking wave height  $R$  was directly estimated as its minimum value  $H_0$  from Equation (A2); the average coastline height above the mean sea level  $H_c$  was corrected by the total sea level increase (storm surge + tide)  $H_s$ .

### Appendix C

The 2019–2020 data extracted from the datasets of the Santa Maria di Leuca (Table A11) and Porto Cesareo stations (Figures A10–A13) are reported below (see Section 3.3).

**Table A11.** Wind speed daily average ( $U_a$ ), wind speed daily maximum ( $U_m$ ), and 30 min average wind speed ( $U_{30}$ ) and direction ( $D$ ) at four selected hours. Data recorded by the Santa Maria di Leuca wind gauge (data extracted from [80,81]).

Storm	Ua	Um	00:00		06:00		12:00		18:00	
			U <sub>30</sub>	D						
12 November 2019 <sup>1</sup>	8.5	24.0	9.8	106°	18.1	107°	13.4	145°	11.7	164°
13 November 2019 <sup>1</sup>	6.0	19.8	15.4	169°	12.7	167°	12.1	173°	4.3	172°
24 November 2019	5.5	19.3	4.9	145°	7.4	129°	14.5	107°	16.3	112°
22 December 2019	4.9	18.1	8.2	191°	9.4	179°	14.0	222°	7.8	259°
2 March 2020	3.7	12.7	7.4	153°	3.0	53°	6.1	139°	8.3	146°

<sup>1</sup> storm Detlef.

During a marine storm, wind speed is significantly higher over the sea than land, while wind direction is affected by more or less apparent changes in crossing the coastline. Land station measurements of wind speed can be halved in comparison with offshore values [88,89]. However, it must be noted that the Santa Maria di Leuca station has an elevation of 26 m a.s.l. and is placed about 100 m inland, while the Porto Cesareo station has an elevation of 12 m a.s.l. and is placed few tens of meters inland. Since the two stations are close to the coastline, the anemometric values reported above can be considered

as indicative for the nearshore conditions. The consistency with the wind speed values extracted from the GLOBO-BOLAM-MOLOCH model cascade (Table 2) confirms the above.

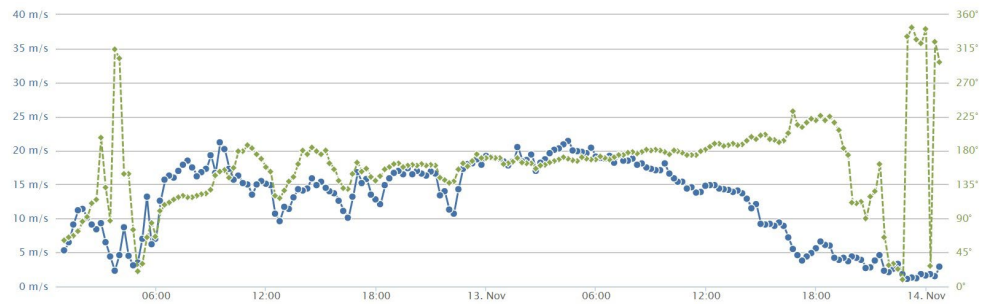


**Figure A10.** Wind speed and direction (dashed line) recorded by the Porto Cesareo wind gauge during storm Detlef; image downloaded 13 November 2023 from the site of the Apulian Meteomarine Network [83].

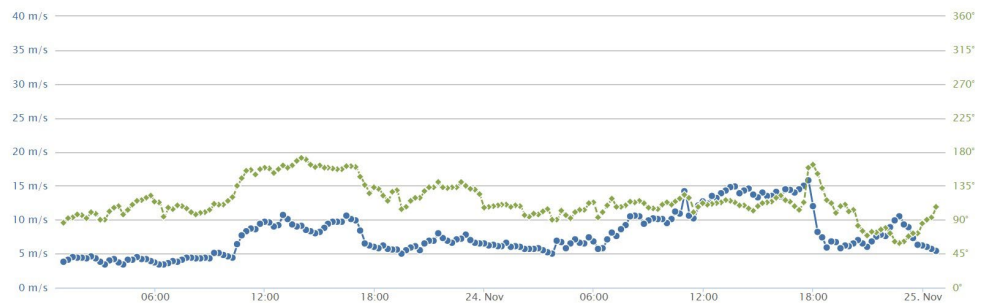


**Figure A11.** Wind speed and direction (dashed line) recorded by the Porto Cesareo wind gauge during the 24 November 2019 storm; image downloaded 13 November 2023 from the site of the Apulian Meteomarine Network [83].

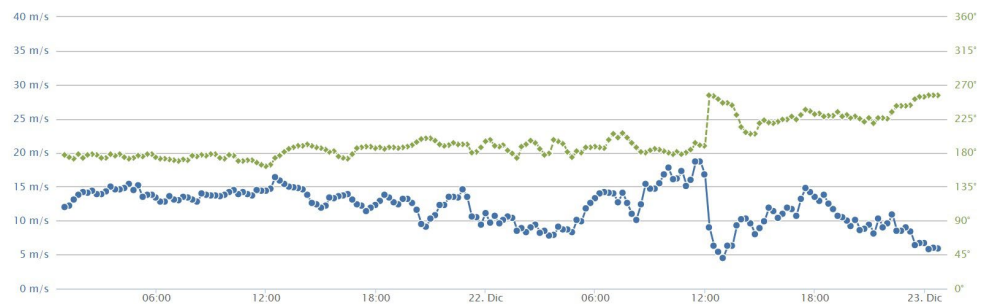


**Figure A12.** Wind speed and direction (dashed line) recorded by the Porto Cesareo wind gauge during the 22 December 2019 storm; image downloaded 13 November 2023 from the site of the Apulian Meteomarine Network [83].

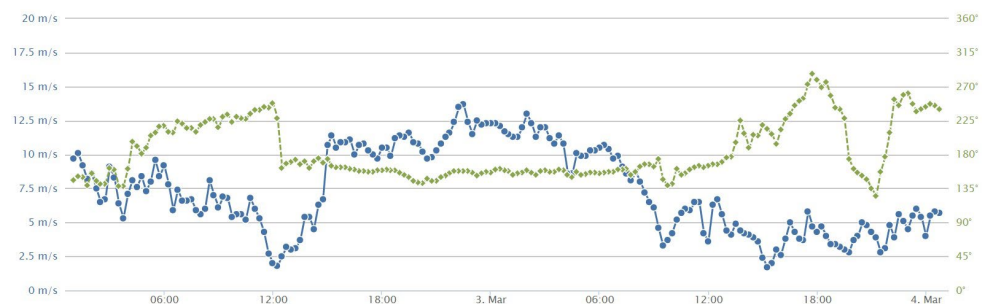


**Figure A13.** Wind speed and direction (dashed line) recorded by the Porto Cesareo wind gauge during the 2 March 2020 storm; image downloaded 13 November 2023 from the site of the Apulian Meteomarine Network [83].

## Appendix D

By using the storm power index (SPI) introduced by Dolan and Davis [90], the intensity of the storms reported in Table 2 can be calculated. SPI is defined as the “*storm’s duration times the square of maximum significant wave height*” [90]. A number of studies have shown a strong correlation between SPI and the wave impact on the coasts (see, e.g., [91–93]). Considering that  $H_0$  is nearly equivalent to the significant wave height [76,77], the storm intensities can be assessed as reported in Figure A14.

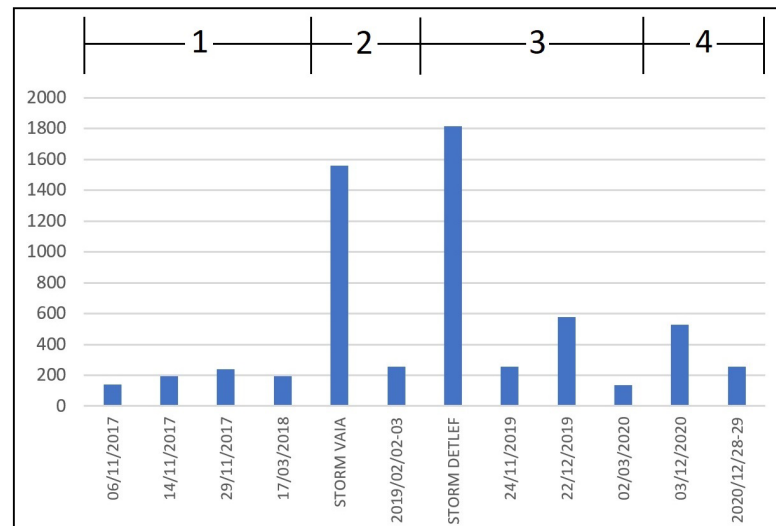


**Figure A14.** Storm power index (in m<sup>2</sup> h) of the storms in Table 2. Annual intervals of Table 3 are reported in the upper side.

Considering the obtained values of SPI, the quite different ability of the two most severe storms to determine geomorphological signatures in the study area is surprising. It can be guessed that the interplay between wind speed and length and duration in time of the fetch involved can determine a sort of threshold-like behavior between storms that do not cause massive changes (including Vaia) and the most intense one (Detlef). Some insights into the reasons for the different effects of the two storms on the studied coast were discussed in Delle Rose and Martano [4] and Delle Rose et al. [9].

As stated above (Section 4.3), some boulders displaced during the interval 3 (Table 3) could be caused by the storms that occurred between 24 November 2019 and 2 March 2020 (Figure 10). Considering Figure A14, the storm that occurred on 22 December 2019 (SPI about 580) seems to be the main suspect. However, considering that storm Vaia (SPI about 1570) was able to move only one of the detected boulders (Section 3.2), this probability is rather low. On the other hand, the 3 December 2020 storm can be considered the most probable cause for the two displacements that occurred during the interval 4 (Table 3).

The strong power of storm Detlef on the eastern coast of the Gulf of Taranto is supported also by the resulting damage [17,21]. Promenade walls were destroyed and breakwater blocks displaced toward the coastal roads. The most affected places were Porto Cesareo, Santa Caterina, and Gallipoli (Figure 1). In the last town, several boats sunk, and numerous infrastructures along the seafront were destroyed. Differently, no damage was reported for the other considered storms.

A quantitative comparison with other phenomena of boulder displacements can help to better understand the work caused by storm Detlef on the studied coast. Several authors used the minimum flow velocity  $V$  to set the boulders in motion [1,71] as a measure of the nearshore wave energy (see, e.g., [48,86,94]). For the biggest displaced boulders herein considered,  $V$  ranges from 2.7 to 8.1 m/s (Table A12).

**Table A12.** Minimum flow velocity ( $V$ ) (in m/s) required to set the boulders in motion;  $a_f$ ,  $b_f$ ,  $c_f$ ,  $x_i$ , and TD (in m).  $V$  was computed with the equations of Nandasena et al. [1,71]. Note: See caption of Table A2 for abbreviations.

Boulder ID	Size ( $a_f \times b_f \times c_f$ )	$x_i$	TD	PTS	MT	$V$
PRq <sup>1</sup>	2.7 × 1.4 × 0.4	1.9	11.7	SA	ST	5.9
SIg <sup>1</sup>	1.7 × 1.5 × 0.5	9	2.4	SA	OV	4.4
SCb	1.8 × 1.6 × 0.7	18.8	15.4	SA	OV	5.4
PIh <sup>1</sup>	3.1 × 2.2 × 0.4	1.7	14.3	SA	ST	5.9
MAa <sup>1</sup>	3.4 × 2.1 × 0.5	0.6	4.4	SA	SL	2.8
SUa <sup>1</sup>	5.4 × 4.6 × 1.9	0	8.9	SB	SL	4.4
CAd <sup>1</sup>	2.6 × 2.4 × 0.9	3.9	2.5	SA	OV	5.6
PILj	3.0 × 1.8 × 0.6	0.7	1.6	SB	SL	2.7
ROd	2.4 × 1.5 × 0.7	10.4	4.5	SA	OV	4.3
ROn	2.8 × 2.1 × 0.5	4.2	17.1	SA	ST	6.6
SGe	2.2 × 1.7 × 0.7	13.8	6.5	SA	ST	7.8
CIc <sup>1</sup>	2.2 × 1.4 × 0.5	5.2	3.3	SA	ST	8.1

<sup>1</sup> Boulder detected by [9]; the MAa boulder, considered JB by [9], is here considered SA (see Appendix A).

Values of  $V$  up to 14 m/s were calculated to explain boulder displacements due to inundation events driven by typhoons in the Asia-Pacific region [39,79,94–96]. Instead, for the Mediterranean region,  $V$  values up to 12 m/s are reported in the literature to displace SA or SB boulders by severe storms [1,48]. Therefore, the values in Table A12 appear consistent (in terms of order of magnitude) with those found in the literature.

## References

- Nandasena, N.A.K.; Paris, R.; Tanaka, N. Reassessment of hydrodynamic equations to initiate boulder transport by high energy events (storms, tsunamis). *Mar. Geol.* **2011**, *281*, 70–84. [CrossRef]
- Engel, M.; May, S.M. Bonaire’s boulder field revisited: Evidence for Holocene tsunami impact on the Leeward Antilles. *Quat. Sci. Rev.* **2012**, *54*, 126–141. [CrossRef]
- Kennedy, A.B.; Cox, R.; Dias, F. Storm waves may be the source of some “tsunami” coastal boulder deposits. *Geophys. Res. Lett.* **2021**, *48*, e2020GL090775. [CrossRef] [PubMed]
- Delle Rose, M.; Martano, P. The Imprint of Recent Meteorological Events on Boulder Deposits along the Mediterranean Rocky Coasts. *Climate* **2022**, *10*, 94. [CrossRef]
- Collin, A.; Etienne, S.; Planes, S. High-energy events, boulder deposits and the use of very high resolution remote sensing in coral reef environments. *J. Coast. Res. Spec. Issue* **2013**, *65*, 690–695. [CrossRef]
- Collin, A.; Etienne, S.; Jeanson, M. Three-dimensional structure of coral reef boulders transported by stormy waves using the very high resolution WorldView-2 satellite. *J. Coast. Res. Spec. Issue* **2016**, *75*, 572–576. [CrossRef]
- Cox, R. Megagravel deposits on the west coast of Ireland show the impacts of severe storms. *Weather* **2020**, *75*, 72–77. [CrossRef]
- Ruban, D.A. Finding Coastal Megaclast Deposits: A Virtual Perspective. *J. Mar. Sci. Eng.* **2020**, *8*, 164. [CrossRef]
- Delle Rose, M.; Martano, P.; Orlanducci, L. Coastal Boulder Dynamics Inferred from Multi-Temporal Satellite Imagery, Geological and Meteorological Investigations in Southern Apulia, Italy. *Water* **2021**, *13*, 2426. [CrossRef]
- Kennedy, D.M.; Woods, J.L.D.; Naylor, L.A.; Hansom, J.D.; Rosser, N.J. Intertidal boulder-based wave hindcasting can underestimate wave size: Evidence from Yorkshire, UK. *Mar. Geol.* **2019**, *411*, 98–106. [CrossRef]
- Hastewell, L.J.; Schaefer, M.; Bray, M.; Inkpen, R. Intertidal boulder transport: A proposed methodology adopting Radio Frequency Identification (RFID) technology to quantify storm induced boulder mobility. *Earth Surf. Process. Landf.* **2019**, *44*, 681–698. [CrossRef]
- Gomez-Pazo, A.; Perez-Alberti, A.; Trenhaile, A. Tracking clast mobility using RFID sensors on a boulder beach in Galicia, NW Spain. *Geomorphology* **2021**, *373*, 107514. [CrossRef]
- Autret, R.; Dodet, G.; Suanez, S.; Roudaut, G.; Fichaut, B. Long-term variability of supratidal coastal boulder activation in Brittany (France). *Geomorphology* **2018**, *304*, 184–200. [CrossRef]
- Hoffmeister, D.; Curdt, C.; Bareth, G. Monitoring the sedimentary budget and dislocated boulders in western Greece—Results since 2008. *Sedimentology* **2020**, *67*, 1411–1430. [CrossRef]
- Ferrarin, C.; Valentini, A.; Vodopivec, M.; Klaric, D.; Massaro, G.; Bajo, M.; De Pascalis, F.; Fadini, A.; Ghezzi, M.; Menegon, S.; et al. Integrated sea storm management strategy: The 29 October 2018 event in the Adriatic Sea. *Nat. Hazards Earth Syst. Sci.* **2020**, *20*, 73–93. [CrossRef]

16. Ferrarin, C.; Bajo, M.; Benetazzo, A.; Cavaleri, L.; Chiggiato, J.; Barbariol, F.; Bastianini, M.; Bertotti, L.; Davolio, S.; Magnusson, L.; et al. Local and large-scale controls of the exceptional Venice floods of November 2019. *Prog. Oceanogr.* **2021**, *197*, 102628. [[CrossRef](#)]
17. Delle Rose, M.; Fidelibus, C.; Martano, P.; Orlanducci, L. Storm-induced boulder displacements: Inferences from field surveys and hydrodynamic equations. *Geosciences* **2020**, *10*, 374. [[CrossRef](#)]
18. Morucci, S.; Picone, M.; Nardone, G.; Arena, G. Tides and waves in the central Mediterranean Sea. *J. Oper. Oceanogr.* **2016**, *9*, s10–s17. [[CrossRef](#)]
19. Dentale, F.; Furcolo, P.; Pugliese Carratelli, E.; Reale, F.; Contestabile, P.; Tomasicchio, G.R. Extreme wave analysis by integrating model and wave buoy data. *Water* **2018**, *10*, 373. [[CrossRef](#)]
20. Ciricugno, L.; Delle Rose, M.; Fidelibus, C.; Orlanducci, L.; Mangia, M. Sullo spostamento di massi costieri causato da onde “estreme” (costa ionica salentina). *Geol. Territ.* **2019**, *16*, 15–23. (In Italian)
21. Delle Rose, M.; Ciricugno, L.; Fidelibus, C.; Martano, P.; Marzo, L.; Orlanducci, L. Considerazioni geologiche su processi morfodinamici causati sulla costa ionica salentina da recenti tempeste. *Geol. Territ.* **2020**, *18*, 5–15. (In Italian)
22. Spano, D.; Snyder, R.L.; Cesaraccio, C. Mediterranean Climates. In *Phenology: An Integrative Environmental Science*; Schwartz, M.D., Ed.; Springer: Dordrecht, The Netherlands, 2003; pp. 139–156.
23. Lionello, P.; Malanotte-Rizzoli, P.; Boscolo, R.; Alpert, P.; Artale, V.; Li, L.; Luterbacher, J.; May, W.; Trigo, R.; Tsimplis, M.; et al. The Mediterranean Climate: An Overview of the Main Characteristics and Issues. *Dev. Earth Environ. Sci.* **2006**, *4*, 1–26.
24. Zito, G.; Ruggiero, L.; Zuanni, F. Aspetti meteorologici e climatici della Puglia. In Proceedings of the First Workshop on “Clima, Ambiente e Territorio nel Mezzogiorno”, Taormina, Italy, 11–12 December 1989; CNR: Roma, Italy, 1991; pp. 43–73. (In Italian).
25. Mastronuzzi, G.; Pignatelli, C. The boulder berm of Punta Saguerra (Taranto, Italy): A morphological imprint of the Rossano Calabro tsunamis of April 24, 1836? *Earth Planets Space* **2012**, *64*, 829–842. [[CrossRef](#)]
26. Zhao, Q.; Yu, L.; Li, X.; Peng, D.; Zhang, Y.; Gong, P. Progress and Trends in the Application of Google Earth and Google Earth Engine. *Remote Sens.* **2021**, *13*, 3778. [[CrossRef](#)]
27. Goudie, A. Coasts. In *Landscapes of the Anthropocene with Google Earth*; Goudie, A., Ed.; Springer Nature: Cham, Switzerland, 2023; pp. 129–162.
28. Kennedy, A.B.; Mori, N.; Yasuda, T.; Shimozono, T.; Tomiczek, T.; Donahue, A.; Shimura, T.; Imai, Y. Extreme block and boulder transport along a cliffed coastline (Calicoan Island, Philippines) during Super Typhoon Haiyan. *Mar. Geol.* **2017**, *383*, 65–77. [[CrossRef](#)]
29. Medina, F.; Mhammdi, N.; Emran, A.; Hakdaoui, S. A case of uplift and transport of a large boulder by the recent winter storms at Dahomey beach (Morocco). In Proceedings of the IX Symposium on the Iberian Atlantic Margin, Coimbra, Portugal, 4–7 September 2018; p. 2.
30. Haslett, S.K.; Wong, B.R. Reconnaissance survey of coastal boulders in the Moro Gulf (Philippines) using Google Earth imagery: Initial insights into Celebes Sea tsunami events. *Bull. Geol. Soc. Malays.* **2019**, *68*, 37–44. [[CrossRef](#)]
31. Khuwaja, Z.; Arain, J.; Ali, R.; Meghwar, S.L.; Jatoi, M.A.; Shaikh, F.A. Accuracy Measurement of Google Earth Using GPS and Manual Calculations. In Proceedings of the International Conference Sustainable Development in Civil Engineering, Jamshoro, Pakistan, 23–25 November 2017; Mehran University: Jamshoro, Pakistan, 2018; p. 9.
32. Guo, J.; Tu, H.J.; Li, H.; Zhao, Y.; Zhou, J. Horizontal Accuracy Assessment of Google Earth Data Overtypical Regions of Australia Using Worldview. *Int. Arch. Photogramm. Remote Sens. Spatial Inf. Sci.* **2021**, *XLIII-B3-2021*, 763–768.
33. Pulighe, G.; Baiocchi, V.; Lupia, F. Horizontal accuracy assessment of very high resolution Google Earth images in the city of Rome, Italy. *Int. J. Digit. Earth* **2016**, *9*, 1753–8947. [[CrossRef](#)]
34. Guerriero, L.; Di Martire, D.; Calcaterra, D.; Francioni, M. Digital Image Correlation of Google Earth Images for Earth’s Surface Displacement Estimation. *Remote Sens.* **2020**, *12*, 3518. [[CrossRef](#)]
35. Delle Rose, M.; Martano, P. Wind–Wave Conditions and Change in Coastal Landforms at the Beach–Dune Barrier of Cesine Lagoon (South Italy). *Climate* **2023**, *11*, 128. [[CrossRef](#)]
36. Regione Puglia—Area Politiche per la Mobilita e Qualita Urbana—Servizio Assetto del Territorio. Available online: <http://webapps.sit.puglia.it/freewebapps/Idrogeomorfologia/index.html> (accessed on 16 June 2023). (In Italian).
37. Blaschke, T.; Hay, G.J.; Kelly, M.; Lang, S.; Hofmann, P.; Addink, E.; Queiroz Feitosa, R.; van der Merr, F.; van der Werff, H.; van Coillie, F.; et al. Geographic Object-Based Image Analysis—Towards a new paradigm. *J. Photogramm. Remote Sens.* **2014**, *87*, 180–191. [[CrossRef](#)] [[PubMed](#)]
38. Hoffmeister, D. Mapping of subaerial coarse clasts. In *Geological Records of Tsunamis and Other Extreme Waves*; Engel, M., Pilarczyk, J., May, S.M., Brill, D., Garrett, E., Eds.; Elsevier: Amsterdam, The Netherlands, 2020; pp. 169–184.
39. Terry, J.P.; Lau, A.Y.A.; Nguyen, K.A.; Liou, Y.-A.; Switzer, A.D. Clustered, Stacked and Imbricated Large Coastal Rock Clasts on Ludao Island, Southeast Taiwan, and Their Application to Palaeotyphoon Intensity Assessment. *Front. Earth Sci.* **2021**, *9*, 792369. [[CrossRef](#)]
40. Vaccher, V.; Hastewell, L.; Devoto, S.; Corradetti, A.; Mantovani, M.; Korbar, T.; Furlani, S. The application of UAV-derived SfM-MVS photogrammetry for the investigation of storm wave boulder deposits on a small rocky island in the semi-enclosed Northern Adriatic Sea. *Geomat. Nat. Hazards Risk* **2024**, *15*, 2295817. [[CrossRef](#)]
41. Erdmann, W.; Kelletat, D.; Scheffers, A. Boulder transport by storms—Extreme-waves in the coastal zone of the Irish west coast. *Mar. Geol.* **2018**, *399*, 1–13. [[CrossRef](#)]

42. Oetjen, J.; Engel, M.; Pudasaini, S.P.; Schuettrumpf, H. Significance of boulder shape, shoreline configuration and pre-transport setting for the transport of boulders by tsunamis. *Earth Surf. Process. Landf.* **2020**, *45*, 2118–2133. [[CrossRef](#)]
43. Nandasena, N.A.K.; Scicchitano, G.; Scardino, G.; Milella, M.; Piscitelli, A.; Mastronuzzi, G. Boulder displacements along rocky coasts: A new deterministic and theoretical approach to improve incipient motion formulas. *Geomorphology* **2022**, *407*, 108217. [[CrossRef](#)]
44. Blott, S.G.; Pye, K. Particle shape: A review and new methods of characterization and classification. *Sedimentology* **2008**, *55*, 31–63. [[CrossRef](#)]
45. Blair, T.C.; McPherson, J.G. Grain-size and textural classification of coarse sedimentary particles. *J. Sed. Res.* **1999**, *69*, 6–19. [[CrossRef](#)]
46. Noormets, R.; Felton, E.A.; Crook, K.A.W. Sedimentology of rocky shorelines: 2. Shoreline megaclasts on the north shore of Oahu, Hawaii—origins and history. *Sediment. Geol.* **2002**, *150*, 31–45. [[CrossRef](#)]
47. Causon Deguara, J.; Gauci, R. Evidence of extreme wave events from boulder deposits on the south-east coast of Malta (Central Mediterranean). *Nat. Hazards* **2017**, *86*, 543–568. [[CrossRef](#)]
48. Mottershead, D.N.; Soar, P.J.; Bray, M.J.; Hastewell, L.J. Reconstructing boulder deposition histories: Extreme wave signatures on a complex rocky shoreline of Malta. *Geosciences* **2020**, *10*, 400. [[CrossRef](#)]
49. Knight, J.; Burningham, H. Boulder dynamics on an Atlantic-facing rock coastline, northwest Ireland. *Mar. Geol.* **2011**, *283*, 56–65. [[CrossRef](#)]
50. Barbano, M.S.; Pirrotta, C.; Gerardi, F. Large boulders along the south-eastern Ionian coast of Sicily: Storm or tsunami deposit? *Mar. Geol.* **2010**, *275*, 140–154. [[CrossRef](#)]
51. Boccotti, P. *Wave Mechanics for Ocean Engineering*; Elsevier Science: Amsterdam, The Netherlands, 2000; pp. 1–496.
52. Harley, M. Coastal Storm Definition. In *Coastal Storms*; Ciavola, P., Coco, G., Eds.; John Wiley & Sons: Hoboken, NJ, USA, 2017; pp. 1–21.
53. GLOBO-BOLAM-MOLOCH Forecasts. Available online: <https://www.isac.cnr.it/dinamica/projects/forecasts/bolam/> (accessed on 10 September 2023).
54. Nott, J. Waves, coastal boulder deposits and the importance of the pre-transport setting. *Earth Planet. Sci. Lett.* **2003**, *210*, 269–276. [[CrossRef](#)]
55. Noormets, R.; Felton, E.A.; Crook, K.A.W. Sedimentology of rocky shorelines: 3. Hydrodynamics of megaclasts emplacement and transport on a shore platform, Oahu, Hawaii. *Sediment. Geol.* **2004**, *172*, 41–65. [[CrossRef](#)]
56. Nandasena, N.A.K. Perspective of incipient motion formulas: Boulder transport by high-energy waves. In *Geological Records of Tsunamis and Other Extreme Waves*; Nandasena, N.A.K., Engel, M., Pilarczyk, J., May, S.M., Brill, D., Garrett, E., Eds.; Elsevier: Amsterdam, The Netherlands, 2020; pp. 641–659.
57. Carbone, F.; Dutykh, D.; Dudley, J.M.; Dias, F. Extreme wave runup on a vertical cliff. *Geophys. Res. Lett.* **2013**, *40*, 3138–3143. [[CrossRef](#)]
58. Knight, J.; Burningham, H.; Griffiths, D.; Yao, Y. Coastal boulder movement on a rocky shoreline in northwest Ireland from repeat UAV surveys using Structure from Motion photogrammetry. *Geomorphology* **2023**, *440*, 108883. [[CrossRef](#)]
59. Ganas, A.; Briole, P.; Bozionelos, G.; Barberopoulou, A.; Elias, P.; Tsironi, V.; Valkaniotis, S.; Moshou, A.; Mintourakis, I. The 25 October 2018 Mw = 6.7 Zakynthos earthquake (Ionian Sea, Greece): A low-angle fault model based on GNSS data, relocated seismicity, small tsunami and implications for the seismic hazard in the west Hellenic Arc. *J. Geodyn.* **2020**, *137*, 101731. [[CrossRef](#)]
60. Cox, J.C.; Machemehl, J. Overland bore propagation due to overtopping wave. *J. Waterw. Port Coast. Ocean. Eng.* **1986**, *112*, 161–163. [[CrossRef](#)]
61. Cox, R.; Arduin, F.; Dias, F.; Autret, R.; Beisiegel, N.; Earlie, C.S.; Herterich, J.G.; Kennedy, A.; Paris, R.; Raby, A.; et al. Systematic review shows that work done by storm waves can be misinterpreted as tsunami-related because commonly used hydrodynamic equations are flawed. *Front. Mar. Sci.* **2020**, *7*, 4. [[CrossRef](#)]
62. 12 Novembre 2019: Scirocco Impetuoso, Marea Eccezionale a Venezia e Alluvioni al sud Italia con la Depressione “Detlef”. Available online: <http://www.nimbus.it/eventi/2019/191115MareaEccezionaleVenezia.htm> (accessed on 13 June 2023). (In Italian).
63. Melet, A.; Buontempo, C.; Mattiuzzi, M.; Salamon, P.; Baharel, P.; Breyiannis, G.; Burgess, S.; Crosnier, L.; Le Traon, P.Y.; Mentaschi, L.; et al. European Copernicus Services to Inform on Sea-Level Rise Adaptation: Current Status and Perspectives. *Front. Mar. Sci.* **2021**, *8*, 703425. [[CrossRef](#)]
64. Irazoqui Apecechea, M.; Melet, A.; Armaroli, C. Towards a pan-European coastal flood awareness system: Skill of extreme sea-level forecasts from the Copernicus Marine Service. *Front. Mar. Sci.* **2023**, *9*, 1091844. [[CrossRef](#)]
65. GEOS Captures Tropical Cyclone-like System “Trudy” over the Mediterranean Sea. Available online: [https://gmao.gsfc.nasa.gov/research/science\\_snapshots/2020/medicane\\_Trudy.php](https://gmao.gsfc.nasa.gov/research/science_snapshots/2020/medicane_Trudy.php) (accessed on 13 June 2023).
66. Segunda Borrasca con Nombre de la Temporada. La borrasca Bernardo Afectara Especialmente al E de las islas Baleares. Available online: [https://twitter.com/AEMET\\_Esp/status/1193226687611383811](https://twitter.com/AEMET_Esp/status/1193226687611383811) (accessed on 13 June 2023). (In Spanish).
67. Medicane “Trudy” (Detlef, Bernardo) Makes landfall in Algeria. Available online: <https://watchers.news/2019/11/12/medicane/> (accessed on 13 June 2023).
68. Tropical Cyclone Reports (Mediterranean Sea). Subtropical Storm Detlef. 2019. Available online: [http://zivipotty.hu/2019\\_detlef.pdf](http://zivipotty.hu/2019_detlef.pdf) (accessed on 21 July 2023).

69. Miglietta, M.M.; Buscemi, F.; Dafis, S.; Papa, A.; Tiesi, A.; Conte, D.; Davolio, S.; Flaounas, E.; Levizzani, V.; Rotunno, R. A high-impact meso-beta vortex in the Adriatic Sea. *Q. J. R. Meteorol.* **2023**, *149*, 637–656. [CrossRef]
70. Cavaleri, L.; Bajo, M.; Barbariol, F.; Bastianini, M.; Benetazzo, A.; Bertotti, L.; Chiggiato, J.; Ferrarin, C.; Trincardi, F.; Umgiesser, G. The 2019 flooding of Venice and its implications for future predictions. *Oceanography* **2020**, *33*, 42–49. [CrossRef]
71. Nandasena, N.A.K.; Tanaka, N.; Sasaki, Y.; Osada, M. Boulder transport by the 2011 Great East Japan tsunami: Comprehensive field observations and whether model predictions? *Mar. Geol.* **2013**, *346*, 292–309. [CrossRef]
72. Biolchi, S.; Denamiel, C.; Devoto, S.; Korbar, T.; Macovaz, V.; Scicchitano, G.; Vilibic, I.; Furlani, S. Impact of the October 2018 Storm Vaia on Coastal Boulders in the Northern Adriatic Sea. *Water* **2019**, *11*, 2229. [CrossRef]
73. Roig-Munar, F.X.; Martin-Prieto, J.A.; Rodriguez-Perea, A.; Gelabert, B. Gloria storm effects on the coastal boulders East of Minorca (Balearic Islands). *Environ Earth Sci* **2023**, *82*, 176. [CrossRef]
74. Hasselmann, K.; Ross, D.B.; Muller, P.; Sell, W. A parametric wave prediction model. *J. Phys. Oceanogr.* **1975**, *6*, 200–228. [CrossRef]
75. Hsu, S.A. (Ed.) *Coastal Meteorology*; Academic Press: Cambridge, MA, USA, 1988; 260p.
76. Burroughs, L. Wave forecasting by manual methods. In *Guide to Wave Analysis and Forecasting*; World Meteorological Organization, Ed.; Secretariat of World Meteorological Organization: Geneva, Switzerland, 1998; pp. 43–56.
77. Barua, D.K. Wave hindcasting. In *Encyclopedia of Coastal Science*; Finkl, C.W., Makowski, C., Eds.; Springer International Publishing: Berlin/Heidelberg, Germany, 2019; pp. 1859–1864.
78. Regione Puglia. Annali Idrologici. 2017. Available online: <https://protezionecivile.puglia.it/documents/3171874/3243680/annale2017.pdf/> (accessed on 10 September 2023). (In Italian).
79. Regione Puglia. Annali Idrologici. 2018. Available online: <https://protezionecivile.puglia.it/documents/3171874/3243680/annale2018.pdf/> (accessed on 10 September 2023). (In Italian).
80. Regione Puglia. Annali Idrologici. 2019. Available online: <https://protezionecivile.puglia.it/documents/3171874/3243680/annale2019.pdf/> (accessed on 10 September 2023). (In Italian).
81. Regione Puglia. Annali Idrologici. 2020. Available online: <https://protezionecivile.puglia.it/documents/3171874/3243680/annale2020rev2.pdf/> (accessed on 10 September 2023). (In Italian).
82. Regione Puglia. Annali Idrologici. 2021. Available online: <https://protezionecivile.puglia.it/documents/3171874/3243680/annale2021.pdf/> (accessed on 10 September 2023). (In Italian).
83. SIMOP, Sistema Informativo Mete Oceanografico delle coste Pugliesi, Autorita di Bacino della Puglia. Available online: <http://93.51.158.171/web/simop/home> (accessed on 10 September 2023).
84. Bathurst, J.C. Field Measurement of Boulder Flow Drag. *J. Hydraul. Eng.* **1996**, *122*, 167–169. [CrossRef]
85. Rovere, A.; Casella, E.; Harris, D.L.; Lorscheid, T.; Nandasena, N.A.K.; Dyer, B.; Sandstrom, M.R.; Stocchi, P.; D’Andrea, W.J.; Raymo, M.E. Giant boulders and Last Interglacial storm intensity in the North Atlantic. *Proc. Natl. Acad. Sci. USA* **2017**, *114*, 12144–12149. [CrossRef]
86. Terry, J.P.; Karoro, R.; Gienko, G.A.; Wiczorek, M.; Lau, A.Y.A. Giant palaeotsunami in Kiribati: Converging evidence from geology and oral history. *Isl. Arc* **2021**, *30*, e12417. [CrossRef]
87. Huang, S.Y.; Yen, J.Y.; Wu, B.L.; Shih, N.W. Field observations of sediment transport across the rocky coast of east Taiwan: Impacts of extreme waves on the coastal morphology by Typhoon Soudelor. *Mar. Geol.* **2020**, *421*, 106088. [CrossRef]
88. Schwing, F.B.; Blanton, J.O. The use of land and sea based wind data in a simple circulation model. *J. Phys. Oceanogr.* **1984**, *14*, 193–197. [CrossRef]
89. Phillips, M.R.; Rees, E.F.; Thomas, T. Winds, sea levels and NAO influences: An evaluation. *Glob. Planet. Change* **2013**, *100*, 145–152. [CrossRef]
90. Dolan, R.; Davis, E. An intensity scale for Atlantic coast northeast storms. *J. Coast. Res.* **1992**, *8*, 840–853.
91. Mendoza, E.T.; Trejo-Rangel, M.A.; Salles, P.; Appendini, C.M.; Lopez-Gonzalez, J.; Torres-Freyermuth, A. Storm characterization and coastal hazards in the Yucatan Peninsula. *J. Coast. Res.* **2013**, *65*, 790–795. [CrossRef]
92. Anfuso, G.; Rangel-Buitrago, N.; Cortes-Useche, C.; Iglesias Castillo, B.; Gracia, F.J. Characterization of storm events along the Gulf of Cadiz (eastern central Atlantic Ocean). *Int. J. Climatol.* **2016**, *36*, 3690–3707. [CrossRef]
93. Martzikos, N.; Afentoulis, V.; Tsoukala, V. Storm clustering and classification for the port of Rethymno in Greece. *Water Util. J.* **2018**, *20*, 67–79.
94. Terry, J.P.; Dunne, K.; Jankaew, K. Prehistorical frequency of high-energy marine inundation events driven by typhoons in the bay of Bangkok (Thailand), interpreted from coastal carbonate boulders. *Earth Surf. Process. Landf.* **2016**, *41*, 553–562. [CrossRef]
95. May, S.M.; Engel, M.; Brill, D.; Cuadra, C.; Lagmay, A.M.F.; Santiago, J.; Suarez, J.K.; Reyes, M.; Bruckner, H. Block and boulder transport in Eastern Samar (Philippines) during Supertyphoon Haiyan. *Earth Surf. Dynamic.* **2015**, *3*, 543–558. [CrossRef]
96. Terry, J.P.; Goff, J. Strongly aligned coastal boulders on Ko Larn Island (Thailand): A proxy for past typhoon-driven high-energy wave events in the Bay of Bangkok. *Geogr. Res.* **2019**, *57*, 344–358. [CrossRef]

**Disclaimer/Publisher’s Note:** The statements, opinions and data contained in all publications are solely those of the individual author(s) and contributor(s) and not of MDPI and/or the editor(s). MDPI and/or the editor(s) disclaim responsibility for any injury to people or property resulting from any ideas, methods, instructions or products referred to in the content.